



# Assessing possible mutual orbit period change by shape deformation of Didymos after a kinetic impact in the NASA-led Double Asteroid Redirection Test

Masatoshi Hirabayashi<sup>a,\*</sup>, Alex B. Davis<sup>b</sup>, Eugene G. Fahnestock<sup>c</sup>, Derek C. Richardson<sup>d</sup>, Patrick Michel<sup>e</sup>, Andrew F. Cheng<sup>f</sup>, Andrew S. Rivkin<sup>f</sup>, Daniel J. Scheeres<sup>b</sup>, Steven R. Chesley<sup>c</sup>, Yang Yu<sup>g</sup>, Shantanu P. Naidu<sup>c</sup>, Stephen R. Schwartz<sup>h</sup>, Lance A.M. Benner<sup>c</sup>, Petr Pravec<sup>i</sup>, Angela M. Stickle<sup>f</sup>, Martin Jutzi<sup>j</sup>, the DART Dynamical and Physical Properties (WG3) analysis group

<sup>a</sup> Auburn University, 319 Davis Hall, Auburn, AL 36849, United States

<sup>b</sup> University of Colorado Boulder, 429 UCB, Boulder, CO 80309, United States

<sup>c</sup> Jet Propulsion Laboratory, California Institute of Technology, Pasadena, CA 91109, United States

<sup>d</sup> University of Maryland, College Park, MD 20742, United States

<sup>e</sup> Laboratoire Lagrange, Université Côte d'Azur, Observatoire de la Côte d'Azur, CNRS, CS 34229, 06304 Nice Cedex 4, France

<sup>f</sup> Applied Physics Laboratory/The Johns Hopkins University, Laurel, MD 20723, United States

<sup>g</sup> Beihang University, Beijing 100191, China

<sup>h</sup> University of Arizona, Tucson, AZ 85287, United States

<sup>i</sup> Astronomical Institute, Academy of Sciences of the Czech Republic, Fričova 1, CZ-25165 Ondřejov, Czech Republic

<sup>j</sup> Physics Institute, Space Research and Planetary Sciences, University of Bern, Sidlerstrasse 5, 3012 Bern, Switzerland

Received 23 June 2018; received in revised form 1 December 2018; accepted 30 December 2018

Available online 14 January 2019

## Abstract

The Asteroid Impact & Deflection Assessment (AIDA) targets binary near-Earth asteroid (65803) Didymos. As part of this mission, the NASA-led Double Asteroid Redirection Test (DART) will make a kinetic impactor collide with the smaller secondary of Didymos to test kinetic impact asteroid deflection technology, while the ESA-led Hera mission will evaluate the efficiency of the deflection by conducting detailed on-site observations. Research has shown that the larger primary of Didymos is spinning close to its critical spin, and the DART-impact-driven ejecta would give kinetic energy to the primary. It has been hypothesized that such an energy input might cause structural deformation of the primary, affecting the mutual orbit period, a critical parameter for assessing the kinetic impact deflection by the DART impactor. A key issue in the previous work was that the secondary was assumed to be spherical, which may not be realistic. Here, we use a second-order inertia-integral mutual dynamics model to analyze the effects of the shapes of the primary and the secondary on the mutual orbit period change of the system. We first compare the second-order model with three mutual dynamics models, including a high-order inertia-integral model that takes into account the detailed shapes of Didymos. The comparison tests show that the second-order model may have an error of  $\sim 10\%$  for computing the mutual orbit period change, compared to the high-order model. We next use the second-order model to analyze how the original shape and shape deformation change the mutual orbit period. The results show that when the secondary is elongated, the mutual orbit period becomes short. Also, shape deformation of the secondary further changes the

\* Corresponding author.

E-mail address: [thirabayashi@auburn.edu](mailto:thirabayashi@auburn.edu) (M. Hirabayashi).

mutual orbit period. A better understanding of this mechanism allows for detailed assessment of DART's kinetic impact deflection capability for Didymos.

© 2019 COSPAR. Published by Elsevier Ltd. All rights reserved.

*Keywords:* Planetary defense; Asteroid impact hazards; Kinetic impactor; Mutual orbit dynamics; Binary asteroids

## 1. Introduction

Binary near-Earth asteroid Didymos is the target of the Asteroid Impact & Deflection Assessment (AIDA) mission, which is an international collaboration between NASA and ESA (Cheng et al., 2016, 2018; Michel et al., 2016, 2018). In this mission, NASA leads the Double Asteroid Redirection Test (DART) mission in which a kinetic impactor will be launched to Didymos. As of May 14, 2018, the launch period will be opened after June 15, 2021, and the spacecraft will conduct a flyby of asteroid 2001 CB21 and collide with the smaller secondary of Didymos on October 5, 2022, which is the apparition of Didymos. The DART impactor will have the Didymos Reconnaissance and Asteroid Camera for OpNav (DRACO) visible imager, which will take high-resolution images of the surface of the secondary right before the impact (Cheng et al., 2018). On the other hand, ESA leads the Hera mission, which will send a spacecraft to Didymos to observe the physical properties of this asteroid. The currently planned instruments onboard the Hera spacecraft include the Asteroid Framing Camera (AFC), a Light Detection And Ranging (LIDAR) instrument, and a six-unit CubeSat carrying two instruments: one being the Asteroid SPECTral (ASPECT) imaging instrument, and the other being chosen from radio science, seismology, gravimetry, or volatile detection (Michel et al., 2018). The planned launch date of the Hera spacecraft is October 2023.

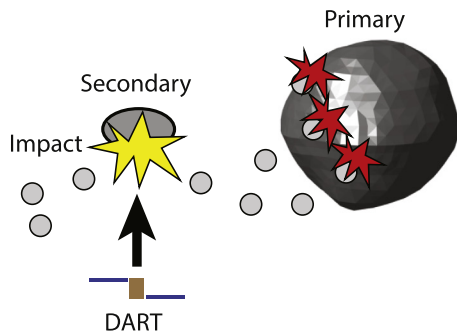
One of the primary goals of the AIDA mission is to quantify the asteroid deflection capability using a kinetic impactor. A critical process is the momentum transfer, which is augmented by impact-driven ejecta (Holsapple and Housen, 2012). The efficiency of the momentum transfer is described using the so-called  $\beta$  parameter. When  $\beta = 1$ , the impactor collides with the asteroid without net generation of momentum-enhancing ejecta so that its momentum is transferred only to the target. If  $\beta > 1$ , the target asteroid achieves further acceleration compared to the  $\beta = 1$  case because the momentum carried by the ejecta launched in the opposite direction to the DART impact direction is added to that of the secondary. On the other hand, if  $\beta < 1$  (requiring antipodal spallation, which is not anticipated for the DART impact), it is accelerated less than the  $\beta = 1$  case. In the AIDA mission, the DART mission demonstrates kinetic impact deflection, determines the mutual orbit period change of Didymos using Earth-based observations and images from the DRACO imager, and attempts to obtain an estimate of the  $\beta$  value (Cheng

et al., 2018). The Hera mission further assesses the  $\beta$  parameter by determining the physical properties including the mass of Didymos (Michel et al., 2018).

Determination of the  $\beta$  parameter requires detailed evaluation of the mutual dynamics and structural condition of Didymos. A study that conducted impact experiments with aluminum spheres hitting pumice boulders showed that the  $\beta$  parameter ranged between 1 and 1.69 (Walker et al., 2017). The  $\beta$  parameter is dependent on the surface topography (Feldhacker et al., 2017) and surface material conditions such as porosity (Wünnemann et al., 2006; Collins, 2014; Wiggins et al., 2018) and regolith size frequency distributions (Tatsumi and Sugita, 2018; Stickle et al., 2018). Such impact conditions likely change the ejecta conditions such as the speed and direction. Therefore, while a fraction of the DART-impact-driven ejecta may fall onto the surface of the primary (Yu et al., 2017; Yu and Michel, 2018), its amount is strongly dependent on these impact conditions. Also, the primary is rotating at a spin period of 2.26 h (Pravec et al., 2006). Given a top-like shape (an oblate shape with a raised equatorial ridge), the primary might be sensitive to failure of the internal structure, depending on the bulk density and material heterogeneity (Zhang et al., 2017). If the primary has the reported nominal size and bulk density (Naidu et al., 2016; Michel et al., 2016), it should have the mechanical strength to hold the current shape (Hirabayashi et al., 2017). Detailed studies using Soft-Sphere Discrete Element Methods (SSDEMs) have been conducted in multiple research groups, which consistently confirmed the result by Hirabayashi and Scheeres (2014), who pointed out that given a uniform structure, a spheroidal shape might have two distinguishable deformation modes: horizontally outward deformation on the equatorial plane and vertically inward deformation at other locations (e.g. Sánchez and Scheeres, 2012, 2016; Zhang et al., 2017, 2018).

Considering these uncertainties, Hirabayashi et al. (2017) hypothesized that if the DART impact induced shape deformation of the primary, the mutual orbit period change, which is a key parameter for determination of the  $\beta$  parameter, would change significantly (the schematics given in Fig. 1). Using the results from earlier structural works (e.g. Hirabayashi and Scheeres, 2014) to assume that the shape deformation process is axisymmetric along the spin axis of the primary, they investigated how the primary's deformed shape would change the mutual orbit period of the system. They found that the primary's shape deformation process might play a significant role in

**Step 1: The DART impactor hits the secondary, and some ejecta may hit the primary.**



**Step 2: The deformed shapes of the system cause additional mutual orbit perturbation.**

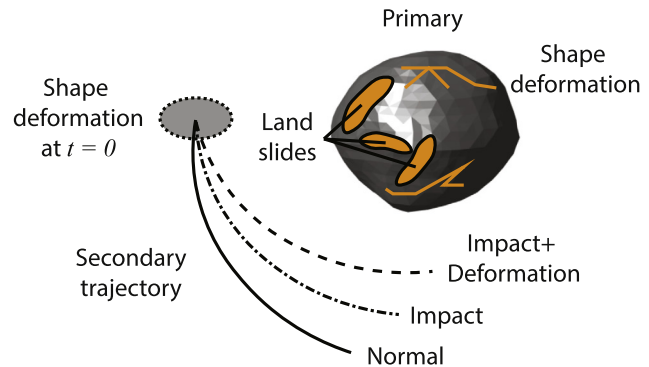


Fig. 1. Schematics of a scenario of the mutual orbit period change caused by shape deformation of Didymos after the DART impact. The shape of the primary used is the radar shape model from Michel et al. (2016) and Naidu et al. (2016). In Step 2, the solid line shows the normal case that experiences neither the DART impact nor shape deformation, the dot-dashed line describes a trajectory after the DART impact without shape deformation, and the dashed line gives a perturbed orbit after the DART impact with shape deformation.

changing the mutual orbit period. However, an issue with their work was that the secondary was assumed to be a perfect sphere although lightcurve observations did not rule out that the secondary would be elongated (Pravec et al., 2006). In fact, many binary asteroids have elongated secondaries (Pravec et al., 2016); therefore, the assumption made by Hirabayashi et al. (2017) might not have accounted for the mutual dynamics of Didymos accurately. We hypothesize that the secondary's elongation also contributes to the mutual orbit period change (Fig. 1) and quantify this problem in the present work.

The purpose of this work is to use a model that takes into account the elongation of the secondary to investigate how the mutual orbit period change would occur in the Didymos system after the DART impact. In our work, we employ a second-order inertia-integral mutual dynamics model in which the shapes of the primary and the secondary are assumed to be an oblate spheroid (i.e., the long axis equal to the intermediate axis) and a prolate ellipsoid (i.e., the intermediate axis equal to the short axis), respectively (Scheeres, 2009; McMahon and Scheeres, 2013). This model is tested by using three approaches capable of computing the mutual orbit period change, which are given below:

- The first is a sphere-sphere dynamics approach that assumes the primary and the secondary to be homogeneous spheres (Cheng et al., 2016).
- The second is a mutual dynamics approach that uses a polyhedron-shape-based gravity model (Werner and Scheeres, 1997) for the primary and assumes the secondary to be a homogeneous sphere (Hirabayashi et al., 2017).
- The third is an inertia-integral-based mutual dynamics approach that takes into account the detailed shapes using high-order gravity terms (Hou et al., 2017; Davis and Scheeres, 2017).

We use the second-order model to analyze how the original shape and shape deformation of Didymos affect the mutual orbit period of the system. The present manuscript contains the following three components:

- First, we generalize the effects of the primary's shape deformation on the mutual orbit period change.
- Second, we investigate how the elongation of the secondary changes the mutual orbit period of the system.
- Third, we explore how the shape deformation process of the secondary influences the mutual orbit period change of the system.

These exercises extend our understanding of the mutual orbit period change of Didymos due to the DART impact from the previous work by Hirabayashi et al. (2017), providing a better capability of quantifying the kinetic impact asteroid deflection by DART.

We organize our discussion as follows. In Section 2, we briefly introduce the model used in this work. In Section 3, we show a deformation process that we consider in the present work. Section 4 presents our numerical investigations. In Section 4.1, we show comparison tests of the second-order model with other mutual dynamics models. In Section 4.2, we discuss how the original shape and shape deformation of the primary and secondary affect the mutual orbit period change of the system. Finally, Section 5 gives interpretations of our numerical results into the mutual orbit period change of Didymos. We note that in the literature, the smaller and larger components of Didymos have been named in different ways (e.g. Michel et al., 2018; Cheng et al., 2018; Hirabayashi et al., 2017). The larger component has been called Didymos, Didymmain, Didymos A, or the primary; on the other hand, the smaller component has been called Didymoon, Didymos B, or the secondary. In this work, we simply call them the primary and the secondary.

## 2. Mutual dynamics modeling

This section introduces the models that are used in this work. We use mathematical notations defined in Table 1. Recall the approaches used are a sphere-sphere model, a polyhedron model, a second-order inertia-integral model, and a high-order inertia-integral model. For the second-order model, the interaction is computed between two biaxial ellipsoids by considering the gravity terms up to second order. This is the main approach used for quantifying the mutual orbit period change due to shape deformation of the system.

### 2.1. Sphere-sphere model

Cheng et al. (2016) introduced the sphere-sphere model. This model considers that both the primary and the secondary are perfectly spherical. In this case, because these objects can be assumed to be point masses, we can use the two-body problem theory. Thus, the rotational motion is independent of the orbital motion. Because this theory has an analytical solution, the orbit period change in the system,  $\delta T_{orbit}$ , can be described as

$$\delta T_{orbit} = 2\pi\sqrt{\frac{\mathcal{A}_a^3}{G(m_p + m_s)}} - 2\pi\sqrt{\frac{\mathcal{A}_b^3}{G(m_p + m_s)}}. \quad (1)$$

In this form,  $\mathcal{A}_b$  and  $\mathcal{A}_a$  are the orbital semi-major axes before and after the DART impact, respectively.  $m_p$  and  $m_s$  are the masses of the primary and the secondary, respectively.  $G$  is the gravitational constant.

### 2.2. Polyhedron-shape-based model

This approach uses a polyhedron-shape gravity model (Werner and Scheeres, 1997) to describe the gravity force acting on the secondary under the assumption that the secondary is perfectly spherical (Hirabayashi et al., 2017). The secondary is considered to have a non-negligible mass; the rotational motion of the primary evolves due to the orbital motion of the components. Therefore, it is necessary to take into account the mutual interaction between the primary and secondary.

The equation of relative translational motion given in the frame rotating with the primary is given as (Scheeres et al., 2006),

$$\ddot{\mathbf{R}}_c + 2\boldsymbol{\Omega}_p \times \dot{\mathbf{R}}_c + \dot{\boldsymbol{\Omega}}_p \times \mathbf{R}_c + \boldsymbol{\Omega}_p \times (\boldsymbol{\Omega}_p \times \mathbf{R}_c) = -\left(1 + \frac{m_s}{m_p}\right) \frac{\partial U}{\partial \mathbf{R}_c}, \quad (2)$$

where  $\mathbf{R}_c$  is the center of mass (COM) of the secondary relative to that of the primary,  $U$  is the potential energy, and  $\boldsymbol{\Omega}_p$  is the spin vector of the primary. As discussed above, the rotational state of the primary is coupled with the orbital motion. Therefore, we describe it as

$$\mathbf{I}_p \dot{\boldsymbol{\Omega}}_p + \boldsymbol{\Omega}_p \times \mathbf{I}_p \boldsymbol{\Omega}_p = \boldsymbol{\tau}_p, \quad (3)$$

where  $\mathbf{I}_p$  is the inertia tensor of the primary, and  $\boldsymbol{\tau}_p$  is the torque acting on the primary.

### 2.3. Second-order inertia-integral model

This model assumes that the primary is an oblate spheroid, and the secondary is a prolate ellipsoid, instead of con-

Table 1

Notational definitions of key parameters used in this work. Subscript  $\mathcal{K}$  is replaced with either  $p$  or  $s$ , where  $p$  stands for the primary and  $s$  indicates the secondary. The COM stands for the center of mass.

Parameters	Symbols	Units
Gravitational constant (= $6.674 \times 10^{-11}$ )	$G$	$\text{m}^3 \cdot \text{kg}^{-2} \cdot \text{s}^{-2}$
Orbital semi-major axis	$\mathcal{A}$	m
Geometric semi-major axis of a body	$a_{\mathcal{K}}$	m
Mass	$m_{\mathcal{K}}$	kg
Position of small element in a body relative to its COM	$\mathbf{r}_{\mathcal{K}}$	m
Force	$\mathbf{f}_{\mathcal{K}}$	N
Torque	$\boldsymbol{\tau}_{\mathcal{K}}$	N·m
Inertia tensor	$\mathbf{I}_{\mathcal{K}}$	$\text{kg} \cdot \text{m}^2$
Spin vector	$\boldsymbol{\Omega}_{\mathcal{K}}$	$\text{rad} \cdot \text{s}^{-1}$
Rotational angle	$\theta_{\mathcal{K}}$	rad
Speed of synchronous orbit	$v_{syn}$	$\text{m} \cdot \text{sec}^{-1}$
Moment of inertia along the out-of-plane direction	$I_{\mathcal{K}z}$	$\text{kg} \cdot \text{m}^2$
Ratio of primary semi-minor axis to semi-major axis	$\chi$	[-]
Ratio of secondary semi-minor axis to semi-major axis	$\zeta$	[-]
Position of secondary COM relative to primary COM	$\mathbf{R}_c$	m
Position of small element in secondary relative to one in primary	$\mathbf{R}$	m
Position of small element in secondary relative to primary COM	$\mathbf{R}^*$	m
Position of secondary COM relative to primary COM in inertial frame	$[\mathbf{R}_{cx}, \mathbf{R}_{cy}, 0]$	m
Total energy	$E$	J
Kinetic energy	$K$	J
Potential energy	$U$	J
Out-of-plane component of system angular momentum	$H$	$\text{kg} \cdot \text{m}^2 \cdot \text{s}^{-1}$

sidering particular shapes (Fig. 2). By an oblate spheroid, we mean that the object’s semi-major axis is the same as its intermediate axis. On the other hand, for the prolate ellipsoid, the semi-minor axis is the same as the semi-intermediate axis. While this assumption may not be realistic, the proposed model may be useful to quantify the mutual orbit period change given the fact that there may remain observational uncertainties of the physical properties of Didymos after the DART impact.

To describe the mutual gravity force, we use an inertia integral, which is given as (Hou et al., 2017; Davis and Scheeres, 2017)

$$T_{\mathcal{K}}^{i,j,k} = \int_{m_{\mathcal{K}}} x_{\mathcal{K}}^i y_{\mathcal{K}}^j z_{\mathcal{K}}^k dm_{\mathcal{K}}, \quad (4)$$

where subscript  $\mathcal{K}$  is replaced with either  $p$  (primary) or  $s$  (secondary). Also,  $(x_{\mathcal{K}}, y_{\mathcal{K}}, z_{\mathcal{K}})^T$  is the position vector of a body element from the COM in its body-fixed frame (see the details in Fig. 3). For the  $n$ th-order inertia integral,  $i + j + k = n$  should be satisfied. We expand the gravity force vector acting on the secondary,  $f_s$ , which is given as

$$f_s = -G \int_p \int_s \frac{\mathbf{R}}{R^3} dm_p dm_s. \quad (5)$$

where  $\mathbf{R}$  is the position vector of a body element in the secondary with respect to one in the primary, and  $R$  is its magnitude. In our model, we consider the inertia integrals up to second order, i.e.,  $n = 2$ . Earlier works considered the moment of inertia, instead of the inertia integrals, to expand Eq. (5) although these models are fundamentally equal because of the order of expansion (Scheeres, 2009; McMahon and Scheeres, 2013).

We focus on the planar motion as the motion in the out-of-plane direction is expected to be small even after the DART impact (Cheng et al., 2016; Hirabayashi et al., 2017). This consideration is also reasonable for the high-order model. In our problem, the high-order model shows that the ratio of the  $z$  component to the norm of the  $x$  and  $y$  components is less than 0.007 % even if we account for the  $z$  component of the DART impact velocity. Using  $\mathbf{R}_c$  and  $f_s$ , we describe the equation of relative translational motion in the inertial frame as

$$\ddot{\mathbf{R}}_c = \left( \frac{1}{m_p} + \frac{1}{m_s} \right) f_s. \quad (6)$$

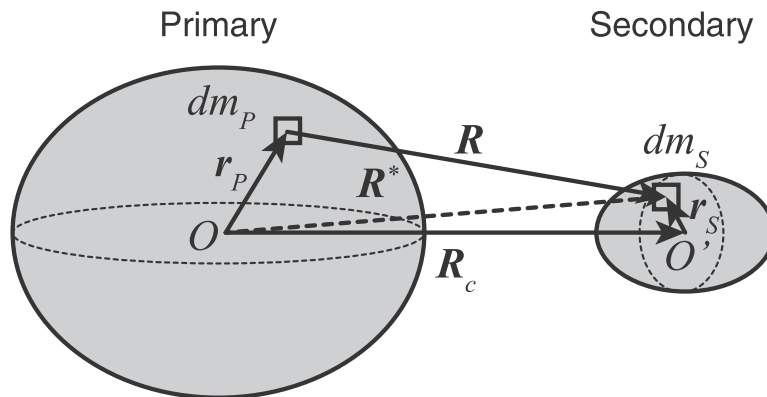


Fig. 2. Illustration of the formulation. In the second-order model, the primary has an oblate shape while the secondary is a prolate ellipsoid.

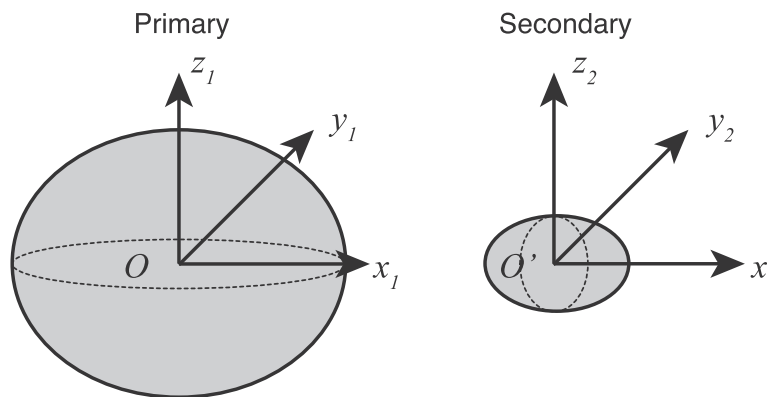


Fig. 3. Illustration of the axis orientations of the primary and the secondary. For the primary, the  $z_1$  axis is defined in the out-of-plane direction, which corresponds to the maximum principal axis of this object, and the  $x_1$  and  $y_1$  axes are on the orbital plane. Similarly, for the secondary, the  $z_2$  axis is equal to its maximum principal axis and is parallel to the  $z_1$  axis. The  $x_2$  axis is defined along the minimum principal axis, and the  $y_2$  axis is along the intermediate principal axis.

On the other hand, the equation of rotational motion in the frame rotating with the secondary is described as

$$\mathbf{I}_s \dot{\boldsymbol{\Omega}}_s + \boldsymbol{\Omega}_s \times \mathbf{I}_s \boldsymbol{\Omega}_s = \boldsymbol{\tau}_s, \tag{7}$$

where  $\mathbf{I}_s$  is the inertia tensor,  $\boldsymbol{\Omega}_s$  is the spin vector, and  $\boldsymbol{\tau}_s$  is the torque vector acting on the secondary. In the present model, because the primary is an oblate shape, its rotational motion can be decoupled with our consideration (see below).

We further discuss our formulation by using the schematics in Fig. 2.  $O$  and  $O'$  are the COMs of the primary and the secondary, respectively. We also define  $\mathbf{R}^*$  to describe the position vector from  $O$  to a small element in the secondary. Vector  $\mathbf{r}_\mathcal{C}$  describes the position vector of a body element from the COM. We expand Eq. (5) by using the following expressions,

$$\mathbf{R} = \mathbf{R}^* - \mathbf{r}_p, \tag{8}$$

$$\mathbf{R}^* = \mathbf{R}_c + \mathbf{r}_s, \tag{9}$$

to obtain

$$R^2 = R^{*2} + r_p^2 - 2\mathbf{R}^* \cdot \mathbf{r}_p, \tag{10}$$

$$R^{*2} = R_c^2 + r_s^2 + 2\mathbf{R}_c \cdot \mathbf{r}_s. \tag{11}$$

We then employ the Taylor expansions of these forms with respect to  $x^* = (r_p^2 - 2\mathbf{R}^* \cdot \mathbf{r}_p)/R^{*2}$  for Eq. (10) and  $x_c = (r_s^2 + 2\mathbf{R}_c \cdot \mathbf{r}_s)/R_c^2$  for Eq. (11).

Applying these formulations, we compute  $\mathbf{f}_s$  and  $\boldsymbol{\tau}_s$ . We first compute the gravity force from the entire mass of the primary acting on a small element in the secondary. This force, denoted as  $d\mathbf{f}_s$ , is given as

$$d\mathbf{f}_s = -Gdm_s \int_{m_p} \frac{\mathbf{R}}{R^3} dm_p. \tag{12}$$

Using Eq. (10), we expand Eq. (12) with respect to  $x^*$ . Considering the terms up to second order, we obtain

$$d\mathbf{f}_s = -\frac{Gdm_s}{R^{*3}} \int_{m_p} \left( 1 - \frac{3}{2}x^* + \frac{15}{8}x^{*2} \right) (\mathbf{R}^* - \mathbf{r}_p) dm_p. \tag{13}$$

We integrate Eq. (13) over the entire mass of the primary. Because the primary is an oblate spheroid, its rotation around the short axis does not affect the gravity acting on any elements in the secondary. In other words, the gravity is independent of the spin of the primary. We describe the motion of the system in the inertial frame. In this frame,  $\mathbf{R}^*$  is given as  $(R_x^*, R_y^*, R_z^*)^T$ , and we obtain

$$d\mathbf{f}_s = -\frac{Gm_p dm_s}{R^{*3}} \left[ \mathbf{R}^* - \frac{3a_p^2}{10} \frac{\mathbf{A}_p \mathbf{R}^*}{R^{*2}} + \frac{3a_p^2}{2} \{ (R_x^{*2} + R_y^{*2}) + \chi^2 R_z^{*2} \} \frac{\mathbf{R}^*}{R^{*4}} \right], \tag{14}$$

where  $a_p$  is the geometric semi-major axis of the primary,  $\chi$  is the primary's oblateness, i.e., the ratio of the short axis to the long axis, and  $\mathbf{A}_p$  is a matrix defined as

$$\mathbf{A}_p = \begin{bmatrix} 4 + \chi^2 & 0 & 0 \\ 0 & 4 + \chi^2 & 0 \\ 0 & 0 & 2 + 3\chi^2 \end{bmatrix}. \tag{15}$$

The primary's rotation does not change this matrix.

The next step is to integrate Eq. (14) over the entire mass of the secondary. It is necessary to consider the attitude of the secondary. Because we prefer to describe the secondary's inertia integrals in the frame fixed on the secondary, we use a transformation process from the body-fixed frame to the inertial frame. We obtain the second-order form of the gravity force acting on the secondary as

$$\begin{aligned} \mathbf{f}_s &= \int_s d\mathbf{f}_s, \\ &\approx -\frac{Gm_p m_s}{R_c^3} \left[ \mathbf{R}_c + \frac{3a_p^2(1-\chi^2)}{10} \frac{\mathbf{U}\mathbf{R}_c}{R_c^2} \right. \\ &\quad \left. + \left\{ \frac{3a_p^2 \mathbf{R}_c^T \mathbf{A}_s \mathbf{R}_c \mathbf{I}}{2R_c^4} - \frac{3a_p^2(\delta_s \mathbf{I} + 2\mathbf{A}_s)}{10R_c^2} \right\} \mathbf{R}_c \right]. \end{aligned} \tag{16}$$

where  $a_s$  is the geometric semi-major axis of the secondary,  $\zeta$  is the secondary's elongation, i.e., the ratio of the intermediate axis to the long axis,  $\mathbf{I}$  is the identity matrix,  $\delta_s$  is given as  $\delta_s = 1 + 2\zeta^2$ , and

$$\mathbf{U} = \begin{bmatrix} 1 & 0 & 0 \\ 0 & 1 & 0 \\ 0 & 0 & 3 \end{bmatrix}. \tag{17}$$

This matrix comes from the fact that the primary is an oblate body that is symmetric along the in-plane directions. Thus, it describes a force contrast between the in-plane components and the out-of-plane component. Also,  $\mathbf{A}_s$  is given as

$$\mathbf{A}_s = \begin{bmatrix} \cos^2 \theta_s + \zeta^2 \sin^2 \theta_s & (1 - \zeta^2) \cos \theta_s \sin \theta_s & 0 \\ (1 - \zeta^2) \cos \theta_s \sin \theta_s & \zeta^2 \cos^2 \theta_s + \sin^2 \theta_s & 0 \\ 0 & 0 & \zeta^2 \end{bmatrix}, \tag{18}$$

where  $\theta_s$  is the rotational angle of the secondary in the inertial frame. Because the motion of this system is assumed to be planar, we write  $\mathbf{R}_c$  as  $[R_{cx}, R_{cy}, 0]^T$ , and thus the  $z$  component is always zero in Eq. (16).

Similarly, the second-order expression of the torque acting on the secondary is computed using Eq. (13), which is given as

$$\boldsymbol{\tau}_s = \int_s \mathbf{r}_s \times d\mathbf{f}_s \approx -\frac{3Gm_p m_s a_s^2}{5R_c^5} \mathbf{R}_c \times \mathbf{A}_s \mathbf{R}_c. \tag{19}$$

The equation of rotational motion is then given as

$$\mathbf{I}_s \dot{\boldsymbol{\Omega}}_s + \boldsymbol{\Omega}_s \times \mathbf{I}_s \boldsymbol{\Omega}_s = -\frac{3Gm_p m_s a_s^2}{5R_c^5} \mathbf{R}_c \times \mathbf{A}_s \mathbf{R}_c. \tag{20}$$

Because the primary and secondary are axisymmetric, the rotational motion along the  $x$  and  $y$  axes is always zero. Therefore, only the motion in the  $z$  axis is a critical component in this problem and is given as

$$I_{sz}\dot{\omega}_s = \frac{3Gm_p m_s a_s^2 (1 - \xi^2)}{10R_c^3} \left\{ -2R_{cx}R_{cy} \cos 2\theta_s + (R_{cx}^2 - R_{cy}^2) \sin 2\theta_s \right\}, \quad (21)$$

$$\dot{\theta}_s = \omega_s, \quad (22)$$

where  $I_{sz} = m_s a_s^2 (1 + 2\xi^2)/5$ , and  $\omega_s$  is the spin rate of the secondary.

If the spin state is synchronized with the orbital motion,  $\omega_s$  is constant and identical to the rate of the orbital motion. Considering that the secondary's long axis points towards the COM of the primary, we obtain the orbit speed of the system. Assuming that the mutual gravity force computed from Eq. (16) is balanced with the centrifugal force, we obtain the relative speed when the secondary's rotation is synchronized with its orbit,  $v_{syn}$ , as

$$v_{syn} = \sqrt{\frac{G(m_p + m_s)}{R_c} \left( 1 + \frac{3a_p^2(1 - \chi^2)}{10R_c^2} + \frac{3a_s^2(1 - \xi^2)}{5R_c^2} \right)}. \quad (23)$$

The energy of this system is conserved and described as

$$E = K + U, \quad (24)$$

where  $E$  is the total energy,  $K$  is the kinetic energy, and  $U$  is the potential energy of the system. These quantities are as follows:

$$K = \frac{1}{2} \frac{m_p m_s}{m_p + m_s} (\dot{R}_{cx}^2 + \dot{R}_{cy}^2) + \frac{1}{10} m_s a_s^2 (1 + \xi^2) \omega_s^2, \quad (25)$$

$$U = -\frac{Gm_p m_s}{R_c} + \frac{1}{10} \frac{Gm_p m_s}{R_c^3} a_p^2 (2 + \chi^2) - \frac{3}{10} \frac{Gm_p m_s}{R_c^3} a_p^2 + \frac{1}{10} \frac{Gm_p m_s}{R_c^3} a_s^2 (1 + 2\xi^2) - \frac{3}{10} \frac{Gm_p m_s}{R_c^3} a_s^2 \{ R_{cx}^2 (\cos^2 \theta_s + \xi^2 \sin^2 \theta_s) + 2R_{cx}R_{cy} (1 - \xi^2) \cos \theta_s \sin \theta_s + R_{cx}^2 (\xi^2 \cos^2 \theta_s + \sin^2 \theta_s) \}. \quad (26)$$

For Eq. (25), the first term and the second term on the right-hand side are the translational effect of the relative motion and the rotational effect of the secondary, respectively. We do not consider the rotational effect of the primary because it is independent of the mutual motion in this problem. Also, Eq. (26) is obtained by integrating  $\mathbf{f}_s$  in Eq. (16) with respect to  $\mathbf{R}_c$ . Also, the angular momentum in the out-of-plane direction is given as

$$H = \frac{m_p m_s}{m_p + m_s} (R_{cx} \dot{R}_{cy} - R_{cy} \dot{R}_{cx}) + \frac{1}{5} m_s a_s^2 (1 + \xi^2) \omega_s. \quad (27)$$

Note that this model can only describe the two-dimensional motion if either  $\chi$  or  $\xi$  has a non-unity value. The operations regarding inertia integrals from Eqs. (14)–(16) removed the components for the rotational orientation in the out-of-plane direction to simplify the present discussion. However, because the out-of-plane mode does not contribute to the mutual orbit period change (Cheng et al., 2016; Hirabayashi et al., 2017), we use the derived forms as the second-order model. Also, when  $\chi = \xi = 1$ , this model becomes identical to the sphere-sphere model.

#### 2.4. High-order inertia-integral model

While computational burden increases, including higher-order terms of the inertia integrals in Eq. (4) increases the accuracy of the gravity calculation because this process accounts for the smaller perturbation due to the gravity variation. The model was developed by Hou et al. (2017) and applied to the mutual dynamics of Didymos by Davis and Scheeres (2017). Unlike the second-order model discussed in Section 2.3, this model takes into account the irregular shapes of Didymos (Davis and Scheeres, 2017). In this section, we briefly summarize this high-order gravity calculation technique. We note other models that describe mutual dynamics of irregularly shaped objects (e.g. von Braun, 1991; Maciejewski, 1995; Werner and Scheeres, 2005; Fahnestock and Scheeres, 2006; Richardson et al., 2009; Hirabayashi and Scheeres, 2013; Naidu et al., 2016).

Given the inertia integrals defined in Eq. (4), we obtain the mutual potential of the system. If we consider an infinite number of the order terms, we can describe the mutual potential as (Hou et al., 2017)

$$U = -G \sum_{n=0}^{\infty} \frac{1}{R_c^{n+1}} U_n, \quad (28)$$

where  $U_n$  is the order term of the mutual potential, which is given as

$$U_n = \sum_{k(2)=n-2\lfloor n/2 \rfloor}^n t_k^n \sum_{(i_1, i_2, i_3)(i_4, i_5, i_6)(j_1, j_2, j_3)(j_4, j_5, j_6)} a_{(i_1, i_2, i_3)(i_4, i_5, i_6)}^k b_{(j_1, j_2, j_3)(j_4, j_5, j_6)}^{n-k} e_1^{i_1+i_4} e_2^{i_2+i_5} e_3^{i_3+i_6} T_p^{(i_1+j_1), (i_2+j_2), (i_3+j_3)} T_s^{(i_4+j_4), (i_5+j_5), (i_6+j_6)}, \quad (29)$$

where  $n$  is the order,  $k(2)$  means that  $k$  steps up with a size of 2, and  $\lfloor n/2 \rfloor$  defines the integer part of  $n/2$  (Hou et al., 2017).  $t_k^n$ ,  $a^k$ , and  $b^k$  are recursive parameters.  $e_1$ ,  $e_2$ , and  $e_3$  are the components of the unit vector of  $\mathbf{R}_c$  in the rotating frame. Also,  $T_s'$  means that the inertia integral is given in the frame rotating with the primary. In addition,  $\sum_{q=1}^6 i_q = k$  and  $\sum_{q=1}^6 j_q = n - k$ .

Computation of the inertia integral parameters is accomplished in a parallel manner to spherical harmonics, wherein a shape model is decomposed into a set of tetrahedra assumed to have uniform density, and the inertia integral of each tetrahedron is summed to compute the inertia integrals for a given shape model (Hou et al., 2017). For convenience, the resulting inertia integrals are computed in the rotating frame of each asteroid. Throughout computation of the mutual gravity potential and torques, the inertia integrals of the secondary are rotated into the frame fixed on the primary, which requires additional computation of the inertia integral tensor,  $T_s'$  (Hou et al., 2017). Also, the mutual gravity torques are computed applying a technique that takes partial derivatives of the potential with respect to the components of a direction cosine matrix

and then considers cross products of them with the components of a direction cosine matrix (Maciejewski, 1995; Hou et al., 2017). To describe the mutual motion between the primary and the secondary, we apply the theory of the full two-body problem (e.g. Scheeres, 2002; Fahnstock and Scheeres, 2006).

### 3. Shape deformation modeling

The goal of this research is to analyze how the shape deformation process would change the mutual orbit period after the DART impact as compared to the case without an impact. We add the shape deformation process into the mutual orbit dynamics models described in Section 2. A key issue is that shape deformation highly depends on the DART impact condition and the physical conditions of the primary and the secondary. In this work, instead of proposing the detailed deformation processes, we analyze the mutual orbit period change considering a possible deformation scenario of the primary and the secondary. Importantly, in the following deformation scenario, we assume that the volume is conserved, considering a constant bulk density.

The primary may experience centrifugal-force-driven shape deformation that is induced by collisions of DART-impact-driven ejecta with the surface of the primary. The primary's spin period is reported to be 2.26 h (e.g. Michel et al., 2016), implying that the primary may be close to structural failure, depending on the density and strength (Zhang et al., 2017; Hirabayashi et al., 2017). Once the DART impactor hits the surface of the secondary, ejecta from the DART impact site orbit the system. Some may escape from the system, some may fall back, and the rest may fall on the primary (Yu et al., 2017; Yu and Michel, 2018). Under these conditions, the deformation process of the top-like-shaped primary may be driven by surface shedding (e.g., Walsh et al., 2008) and internal deformation (e.g., Hirabayashi and Scheeres, 2014), a combination of which may make the shape more oblate (Hirabayashi, 2015). Thus, we consider this mechanism to be the main deformation process of the primary. In the mutual dynamics models, we change the oblateness of the primary under constant volume. The second-order model has the oblateness parameter,  $\chi$ , to control this condition, while the polyhedron-shape-based model changes the aspect ratio of the primary under constant volume.

On the other hand, it is reasonable to consider that the secondary's spin state is synchronized with its orbit (Pravec et al., 2006; Pravec et al., 2016). Because the mutual orbit period of the system is 11.92 h (Michel et al., 2016), the spin condition may not contribute to the deformation of the secondary. Instead, the DART impactor may cause the secondary to deform. When the DART spacecraft hits the surface of the secondary, the shock wave propagates through the interior of the secondary. Here, we consider the secondary's deformation only by considering its elongation. In the following discussion, we only use the

second-order model to analyze the effect of the secondary's shape deformation on the mutual orbit period change. Thus, we change the elongation parameter,  $\xi$ , i.e., the ratio of the secondary's semi-minor axis to its semi-major axis, to model the secondary's deformation. If the secondary becomes less elongated after the DART impact,  $\xi$  becomes larger, i.e., closer to 1. If the secondary becomes more elongated,  $\xi$  should be smaller.

We also introduce an assumption that after the DART impact occurs, the bodies immediately change their shapes but keep their original spin rate.<sup>1</sup> However, this assumption may not be reasonable because it may take some time for Didymos to deform completely. Thus, the mutual dynamics interaction during the deformation process may cause additional effects on the mutual orbit period change. We leave this analysis as our future work. We also note that the present work does not take into account the tidal dissipation effect on the mutual dynamics. Shape irregularity in a binary system causes the secondary's libration (Scheeres et al., 2006). The timescale of tidal dissipation is on the order of million years for a binary system whose the primary's size is about a few hundred kilometers (Goldreich and Sari, 2009); however, it is highly dependent on the mass ratio of the system and tidal dissipation and may range from a thousand years to a million years (Jacobson and Scheeres, 2011).

### 4. Results

We use the second-order mutual dynamics model as our main numerical tool to analyze how the shape and shape deformation of Didymos affect the mutual orbit period change. Before discussing the results, we conduct three comparison tests:

- First, we compare the second-order model with the sphere-sphere model.
- Second, we compare the second-order model with the polyhedron-shape-based mutual dynamics model.
- Third, we compare the second-order model with the high-order model. Note that in these comparison tests, we assume  $\beta = 1$ ; in other words, the discussions do not consider that ejecta delivers additional momentum to the secondary.

After these comparison tests, we analyze the shape effects on the mutual orbit period change, considering the following three cases:

- First, we investigate how the mutual orbit period change is affected by the  $\beta$  parameter and shape deformation of the primary.

<sup>1</sup> The DART impactor is planned to hit the center of figure of the secondary, minimizing the torque acting on it (Cheng et al., 2018).



- Second, the mutual orbit period change is discussed considering the shape of the secondary and variations in the  $\beta$  parameter. In this case, we do not take into account the shape deformation process of the secondary.
- Third, we study the effects of shape deformation of the secondary on the mutual orbit period.

The DART impact configuration is given in Fig. 4. The upper panel describes the DART impact configuration displayed from the horizontal view, while the lower panel illustrates the vertical view. The DART impact angle is defined as an angle between the DART spacecraft’s incoming direction and the horizontal direction of the mutual orbit plane. Also, we assume that the secondary’s velocity direction is opposite to the direction of the DART spacecraft incoming velocity projected onto the mutual orbit plane. Note that Section 4.1.2 shows another DART impact case based on the condition introduced by Hirabayashi et al. (2017).

We introduce how to compute the mutual orbit period change from our numerical results. We first simulate the mutual motion before the DART impact for the timespan that is 10 times as long as the original orbit period. Second, we compute the mutual dynamics by taking into account shape deformation of the system for the same simulation period. Third, we calculate the final true anomalies in these cases and find a difference between them. Then, we divide

the difference by 10 to obtain the mutual period change. Note that when we discuss the mutual orbit period change due to shape deformation, we use subscripts  $b$  and  $a$  for the shapes before and after the DART impact, respectively. For example,  $\xi_a$  means the secondary’s elongation after the DART impact, while  $\chi_b$  defines the primary’s oblateness before the DART impact.

#### 4.1. Comparison tests

##### 4.1.1. Comparison of the second-order model with the sphere-sphere model

This section discusses a case in which the primary and secondary are spheres. Cheng et al. (2016) analyzed the mutual orbit period change by considering this condition. To produce results, we use Eq. (1) and the second-order model that sets  $\chi$  and  $\xi$  as unity values. In this comparison test, we first recover the results from Cheng et al. (2016). The  $\beta$  parameter is assumed to be unity, and other parameters from Cheng et al. (2016) are listed in Table 2.

Using the second-order model with  $\chi = \xi = 1$ , we obtain the mutual orbit period change as  $-4.4309$  min (Table 2), which is consistent with Cheng et al. (2016). The minus sign means that the mutual orbit period after the DART impact becomes shorter than the original orbit period. The out-of-plane component of the initial velocity is considered in this case but does not affect the mutual orbit period change, which is consistent with earlier works (Cheng et al., 2016; Hirabayashi et al., 2017). We also use Eq. (1) to obtain the mutual orbit period change as  $-4.4393$  min, which is slightly different from the result from the second-order model. This difference comes from the second-order model that considers a geometric phase angle, i.e., the true anomaly, and averages it over 10 orbit periods to obtain the mutual orbit period change. The eccentricity is no longer zero after the DART impact, indicating that the second-

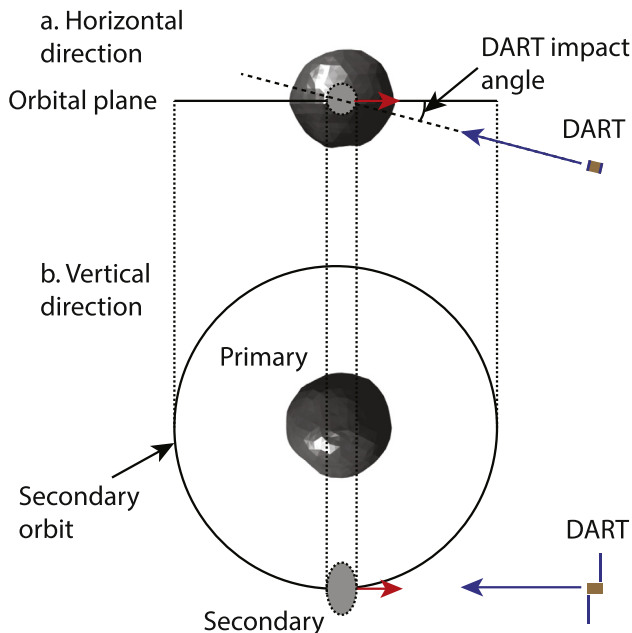


Fig. 4. DART impact conditions. DART impact angle defines an angle between the spacecraft incoming direction and the horizontal direction of the mutual orbit plane. The red arrow and the blue arrow show the velocity vectors of the secondary and the DART impactor, respectively. Assuming the primary and the secondary to be spheres, we obtain the speed of the secondary relative to that of the primary as  $\sim 17.3 \text{ cm}\cdot\text{s}^{-1}$ , which is negligible compared to that of the DART impactor. (For interpretation of the references to colour in this figure legend, the reader is referred to the web version of this article.)

Table 2

Simulation conditions for the case when the primary and the secondary are spheres. The second-order model is used to derive these quantities. The second column describes the simulation condition used by Cheng et al. (2016), while the third column shows the latest impact condition (Cheng, 2018). The minus sign of the mutual orbit period change indicates that the mutual orbit period becomes short after the DART impact. In Parameters, “P” stands for the primary while “S” indicates the secondary.

Parameters	Cheng et al. (2016)	Latest condition	Units
$\beta$ parameter	1.0	1.0	[-]
Initial speed	$1.7281 \times 10^{-1}$	$1.7277 \times 10^{-1}$	$\text{m}\cdot\text{s}^{-1}$
Initial separation	1.18	1.18	km
P initial oblateness	1.0	1.0	[-]
P initial mass	$5.232 \times 10^{11}$	$5.23 \times 10^{11}$	kg
P deformation	No	No	[-]
S initial elongation	1.0	1.0	[-]
S initial mass	$4.8 \times 10^9$	$4.8 \times 10^9$	kg
S deformation	No	No	[-]
DART mass	277	558	kg
DART impact speed	7.030	5.975	$\text{km}\cdot\text{s}^{-1}$
DART impact angle	27.5	15.803	deg
Orbit period change	-4.4309	-8.1832	min

order approach does not correctly provide an accurate value of the mutual orbit period change. However, because the difference is less than 0.2%, we consider this error to be negligible. We confirm that the second-order model used in this work is consistent with the sphere-sphere model developed by Cheng et al. (2016) and thus use the second-order model with  $\chi = \xi = 1$  to produce results for the sphere-sphere model in the following discussion.

We next use the up-to-date values of the DART impact condition as of May 14, 2018 (Cheng, 2018). The neutral mass of the DART impactor is 558 kg, the impact speed is  $5.975 \text{ km}\cdot\text{s}^{-1}$ , and the impact angle is 15.803 deg (Cheng, 2018). This update mainly results from a new implementation of an ion engine thrusting system on the DART spacecraft (Cheng et al., 2018). We use these values to compute the mutual orbit period change (Table 2). Applying the second-order model with  $\chi = \xi = 1$  to the present case, we obtain the mutual orbit period change as  $-8.1832 \text{ min}$ . Therefore, under the assumption of  $\beta = 1$ , the latest prediction of the magnitude of the mutual orbit period change is two times as large as the original prediction (Cheng et al., 2016), which is mainly caused by the change of the DART impactor's mass.

#### 4.1.2. Comparison of the second-order model with the polyhedron-shape-based mutual dynamics model

Here, we compare the second-order model with the polyhedron-shape-based mutual dynamics model developed by Hirabayashi et al. (2017). In this comparison test, to follow the analysis by Hirabayashi et al. (2017), we consider shape deformation of the primary while assuming that the secondary is perfectly spherical. Hirabayashi et al. (2017) analyzed two impact cases to test how the change in the mutual orbit period becomes different due to the direction of the DART impact on the secondary. The first case was when the DART spacecraft collides with the secondary perpendicularly, defined as Case A, (also see Fig. 7 in Hirabayashi et al. (2017)). The second case was when the DART spacecraft experiences a nearly head-on collision, defined as Case B, which is closer to the currently planned DART impact configuration (also see Fig. 6 in Hirabayashi et al. (2017)). In both cases, the DART impact angle is 27.5 deg (Cheng et al., 2016).

To recover the results from Hirabayashi et al. (2017) by using the second-order model, we set up the simulation condition (Table 3). Applying the  $2100\text{-kg}\cdot\text{m}^{-3}$  bulk density used by Hirabayashi et al. (2017), we obtain the components' volumes from their masses. We also define the initial oblateness of the primary,  $\chi_b$ , as 0.939 (Hirabayashi et al., 2017). Note that as discussed before, the second-order model does not consider the out-of-plane mode when either  $\chi$  or  $\xi$  is not unity; however, this effect is negligible (Hirabayashi et al., 2017).

To compare our model with the model by Hirabayashi et al. (2017), we show the mutual orbit period change as a function of the primary's oblateness after the DART impact,  $\chi_a$  (Fig. 5). The magnitude of the mutual orbit period

Table 3

Simulation conditions for the comparison test of the second-order model and the polyhedron-shape-based model.

Parameters	Second-order model	Polyhedron-based model	Units
$\beta$ parameter	1.0	1.0	[-]
Initial speed	$1.7259 \times 10^{-1}$	$1.7278 \times 10^{-1}$	$\text{m}\cdot\text{s}^{-1}$
Initial separation	1.18	1.18	km
P initial mass	$5.12 \times 10^{11}$	$5.12 \times 10^{11}$	kg
P initial bulk density	2100	2100	$\text{kg}\cdot\text{m}^{-3}$
P initial spin period	[-]	2.26	h
P initial oblateness	0.939	[-]	[-]
P initial shape	Spheroid	Didymos	[-]
P deformation	Yes	Yes	[-]
S initial mass	$4.76 \times 10^9$	$4.76 \times 10^9$	kg
S initial bulk density	2100	2100	$\text{kg}\cdot\text{m}^{-3}$
S initial spin period	[-]	[-]	h
S initial elongation	1.0	[-]	[-]
S initial shape	Sphere	Sphere	[-]
S deformation	No	No	[-]
DART mass	500	500	kg
DART impact speed	6	6	$\text{km}\cdot\text{s}^{-1}$
DART impact angle	27.5	27.5	deg

change in Case A is smaller than that in Case B. Because the velocity change in the tangential direction in Case B further pushes the secondary back, the semi-major axis of the system decreases, causing the mutual orbit period to become shorter. These results are consistent overall although the second-order model deviates from the model by Hirabayashi et al. (2017) at  $\chi_a = 0.4$ . This deviation comes from the fact that in contrast to the axisymmetric deformation assumption of the second-order model, shape deformation of the polyhedron shape model may no longer be perfectly symmetric. This discrepancy arises when we compute the true anomalies in these models, providing different mutual orbit period changes.

#### 4.1.3. Comparison of the second-order model with the high-order inertia-integral mutual dynamics model

In this comparison test, we use the second-order model and the high-order inertia-integral mutual dynamics model. We do not take into account shape deformation of the primary and the secondary. Using these two models, we analyze the mutual motion of the system before and after the DART impact. The simulation settings are defined based on the high-order model as it is difficult for us to control the initial conditions due to shape complexity (Table 4). Before discussing this exercise, we show the mutual orbit period change when both the primary and the secondary are spherical. Using the second-order model with  $\chi = \xi = 1$ , we obtain the mutual orbit period change as  $-7.0622 \text{ min}$ .

The high-order inertia-integral mutual dynamics model takes into account the shape of Didymos' primary (Michel et al., 2016; Naidu et al., 2016) and that of 1999 KW4's secondary (Ostro et al., 2006).<sup>2</sup> The inertia integrals

<sup>2</sup> The size of 1999 KW4's secondary is rescaled to fit that of Didymos' secondary.

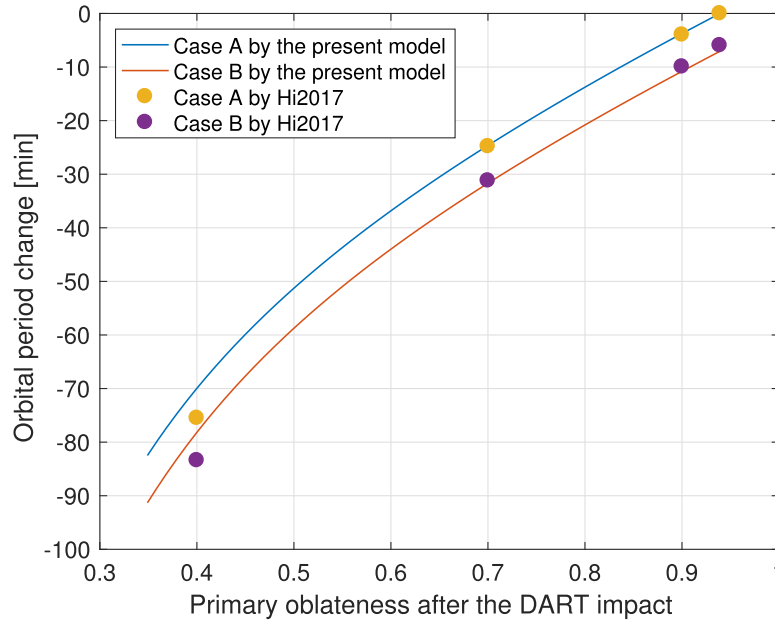


Fig. 5. Comparison between the results from the second-order model and those from the polyhedron-shape-based mutual dynamics model by Hirabayashi et al. (2017). The x axis is the primary’s oblateness after the DART impact,  $\chi_a$ . The secondary is considered to be a perfect sphere. The circles are the results from Hirabayashi et al. (2017). The yellow circles indicate the results in Case A, while the purple circles describe those in Case B. The lines show the results from the second-order model. The blue line shows Case A, while the red line describes Case B. Hi2017 indicates the model used by Hirabayashi et al. (2017). Note that the observationally driven orbital period is 11.92 h (Michel et al., 2016). (For interpretation of the references to colour in this figure legend, the reader is referred to the web version of this article.)

Table 4

Simulation conditions for the comparison test of the second-order model and the high-order model. “Sphere” means the case when the primary and the secondary are perfectly spherical, which is recovered by the second-order model with  $\chi = \xi = 1$ . “High” means the high-order model. “Second” means the second-order model. For the primary’s shape, “Didymos” means the primary of Didymos (Michel et al., 2016; Naidu et al., 2016). For the secondary’s shape, “1999 KW4” means the rescaled secondary of 1999 KW4 (Ostro et al., 2006). In the second-order model, we only consider the horizontal component of the DART impact velocity to avoid the out-of-plane direction.

Parameters	Sphere	High	Second (Case 1)	Second (Case 2)	Second (latest)	Units
$\beta$ parameter	0	0	0	0	0	[-]
Initial speed	$1.7313 \times 10^{-1}$	$1.7313 \times 10^{-1}$	$1.7313 \times 10^{-1}$	$1.7313 \times 10^{-1}$	$1.7278 \times 10^{-1}$	$\text{m}\cdot\text{s}^{-1}$
Initial separation	1.183	1.183	1.183	1.183	1.18	km
P initial mass	$5.2290 \times 10^{11}$	$5.2290 \times 10^{11}$	$5.2290 \times 10^{11}$	$5.2290 \times 10^{11}$	$5.23 \times 10^{11}$	kg
P initial bulk density	2146	2146	2146	2146	2100	$\text{kg}\cdot\text{m}^{-3}$
P initial spin period	[-]	2.26	[-]	[-]	[-]	h
P initial oblateness	1.0	[-]	0.939	0.965	0.965	[-]
P initial shape	Sphere	Didymos	Spheroid	Spheroid	Spheroid	[-]
P deformation	No	No	No	No	No	[-]
S initial mass	$4.9611 \times 10^9$	$4.9611 \times 10^9$	$4.9611 \times 10^9$	$4.9611 \times 10^9$	$4.8 \times 10^9$	kg
S initial bulk density	2146	2146	2146	2146	2100	$\text{kg}\cdot\text{m}^{-3}$
S initial spin period	[-]	11.92	11.92	11.92	11.89	h
S initial elongation	1.0	[-]	0.5765	0.65	0.65	[-]
S initial shape	Sphere	1999 KW4	Ellipsoid	Ellipsoid	Ellipsoid	[-]
S deformation	No	No	No	No	No	[-]
DART mass	500	500	500	500	558	kg
DART impact speed	6	6	6	6	5.975	$\text{km}\cdot\text{s}^{-1}$
DART impact angle	27.5	27.5	27.5	27.5	15.803	deg
Orbit period change	-7.0622	-7.9697	-7.2561	-7.2061	-8.4725	min

are computed up to fourth order based on the accuracy analysis performed by Davis and Scheeres (2017). The initial velocity is selected as the Keplerian orbit velocity. The rotational states of the primary and the secondary are assumed to be in the principal axis mode initially; however, because of the mutual motion, the spin conditions of these

objects immediately deviate from the original states. Based on the parameters given in Table 4, the high-order model gives a mutual orbit period change of -7.9697 min.

We compare this mutual orbit period change with the results from the second-order model. Here, we output the motion in 20 orbit periods. To recover the mutual motion

obtained from the high-order model using the second-order model, we consider two pairs of  $\chi$  and  $\xi$ . The first pair is determined using the geometric conditions of the primary and the secondary. The second pair is obtained attempting to make the mutual motion derived from the second-order model consistent with that from the high-order model. Note that as we showed in Section 2, a difference between these models is that while the second-order model uses ideal shapes (an oblate spheroid and a prolate ellipsoid), the high-order model takes into account detailed shapes of the Didymos system.

We first produce the mutual motion from the high-order model by using the second-order model with geometrically determined  $\chi$  and  $\xi$ . Measuring the aspect ratios of Didymos' primary and 1999 KW's secondary, we obtain  $\chi$  as 0.939 (Michel et al., 2016; Hirabayashi et al., 2017) and  $\xi$

as 0.5765 (Ostro et al., 2006). We compute the mutual orbit period change as  $-7.2561$  min (Case 1). This result has an error within 9%, compared to the mutual orbit period change from the high-order model (Table 4). Compared to the sphere-sphere model that gave the  $-7.0622$ -min change, the second-order model provides a mutual orbit period change of  $-7.2561$  min and make it closer to the estimate by the high-order model, i.e.,  $-7.9697$  min.

However, the mutual motion from the second-order model gradually deviates from that from the high-order model. Figs. 6 and 7 describe the mutual motion in the cases before and after the DART impact, respectively. In each figure, Panel (a) describes the  $x$ -component of the position in the inertial frame (top) and the rotational angle in the inertial frame (bottom), while Panel (b) shows the solutions from the second-order model relative to those

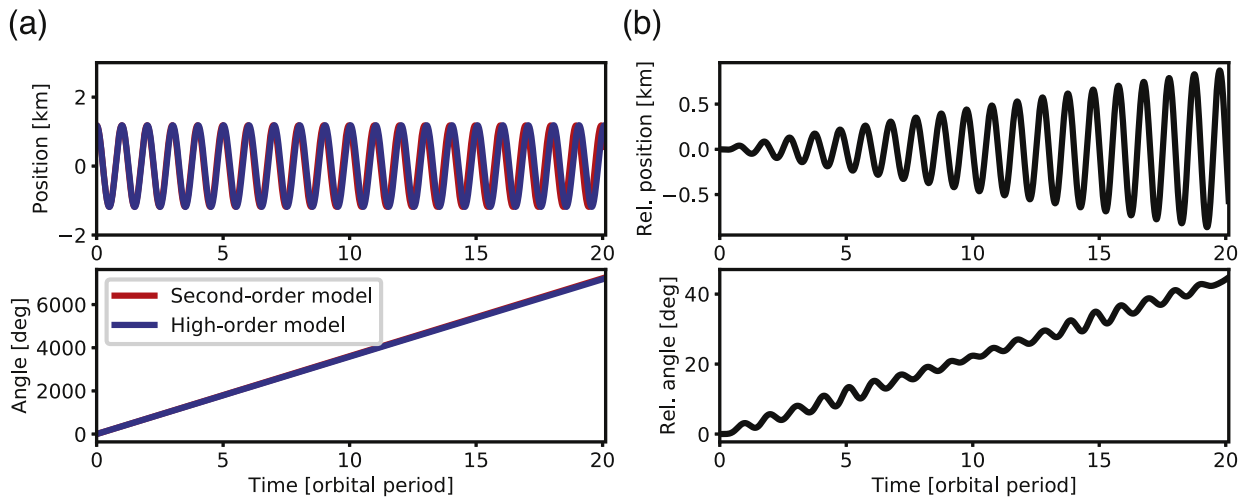


Fig. 6. Numerical simulation comparison of the second-order model and the high-order model. This figure shows the motion *before* the DART impact.  $\chi$  and  $\xi$  are determined using a geometric measurement of the shapes and are defined as 0.939 and 0.5765, respectively. In Panel (a), the top panel describes the position in the  $x$  axis in kilometers, and the bottom panel gives the rotational angle of the secondary in degrees. The red line is the second-order model, while the blue line is the high-order model. Panel (b) provides the differences between the solutions from the two models. (For interpretation of the references to colour in this figure legend, the reader is referred to the web version of this article.)

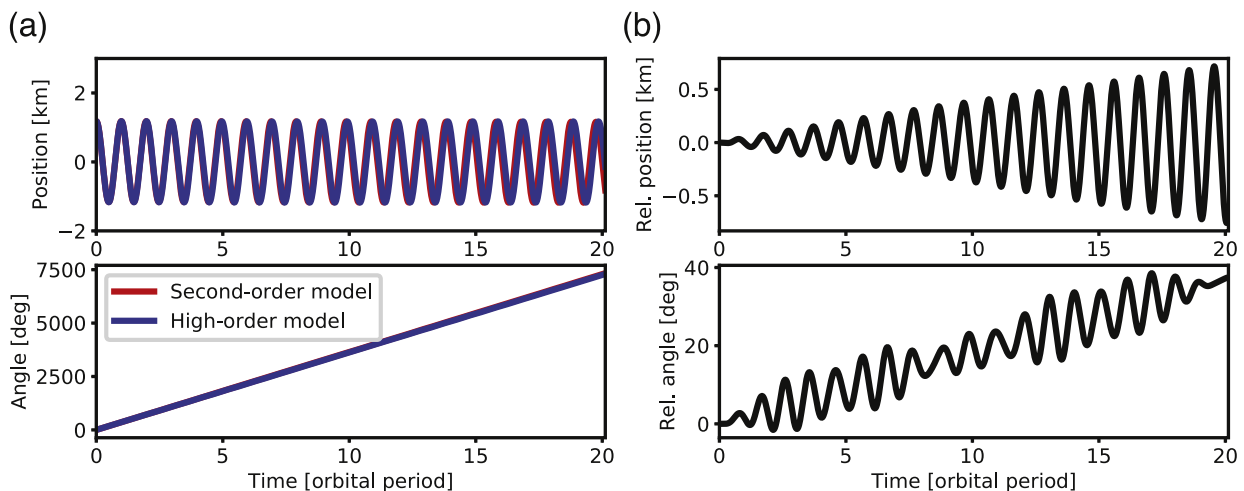


Fig. 7. Numerical simulation comparison of the second-order model and the high-order model. This figure shows the motion *after* the DART impact.  $\chi$  and  $\xi$  are defined as 0.939 and 0.5765, respectively. The format is the same as Fig. 6.

from the high-order model. It is found that the relative translational motion and the rotational motion deviate up to 0.5 km and 40 deg, respectively, after 20 original orbit periods. The error oscillates, and its amplitude gradually increases (Figs. 6 and 7). We interpret this discrepancy as ignorance of the effects of the detailed shapes on the mutual motion in the second-order model.

We next find  $\chi$  and  $\xi$  such that the mutual condition from the second-order model is consistent with that from the high-order model. Finding proper values of  $\chi$  and  $\xi$ , we minimize the difference between the second-order model and the high-order model in the 20-orbit-period simulation time. This case is denoted as Case 2. We find that when  $\chi = 0.965$  and  $\xi = 0.65$ , the deviation becomes minimum. Figs. 8 and 9 describe the results in Case 2. The format is the same as for Figs. 6 and 7. The difference of the rotational angle is less than 10 deg after 20 orbit periods, and

that of the position is about 0.05 km after that time. Using this configuration, we obtain the mutual orbit period change as  $-7.2061$  min, which includes an error of 11%.

The mutual motion in Case 2 is more consistent with the result from the high-order model than that in Case 1; however, the mutual orbit period change in Case 1 is closer to the  $-7.9697$ -min change from the high-order model than that in Case 2. This discrepancy comes from the fact that the second-order model gradually deviates from the high-order model in the cases both before and after the DART impact. These deviations are canceled out when the mutual orbit period change is calculated. We find that tuning on  $\chi$  and  $\xi$  does not improve the mutual orbit period change. This test indicates that the second-order model has an error of  $\sim 10\%$  for the estimate of the mutual orbit period change. Finally, we observe secular perturbation of the relative rotation angle in all the cases (Figs. 6–9). The main

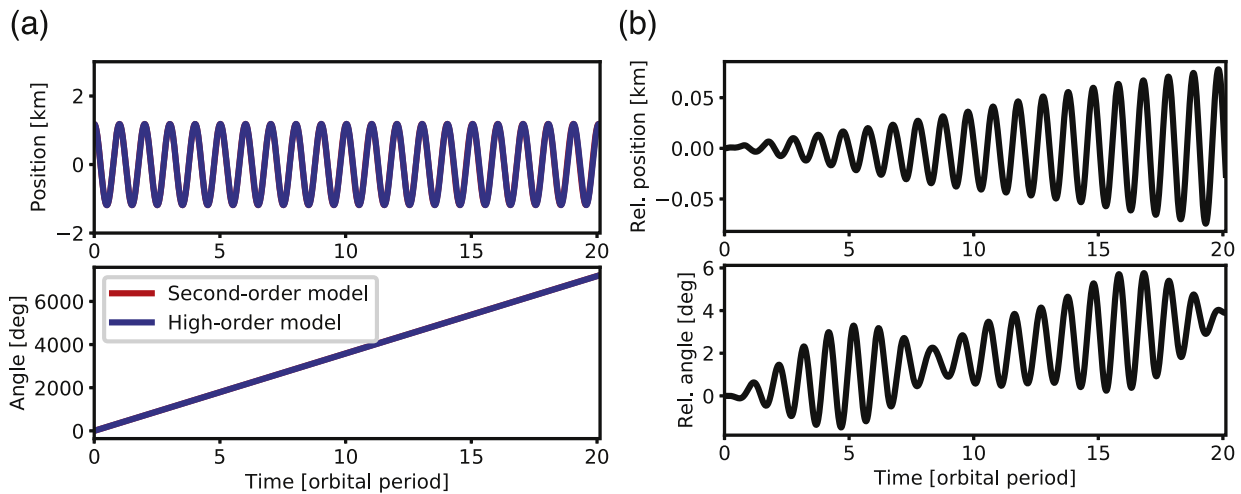


Fig. 8. Numerical simulation comparison of the second-order model and the high-order model. This figure shows the motion *before* the DART impact.  $\chi$  and  $\xi$  are obtained finding the minimum deviation between the second-order model and the high-order model and defined as 0.965 and 0.65, respectively. The format is the same as Fig. 6.

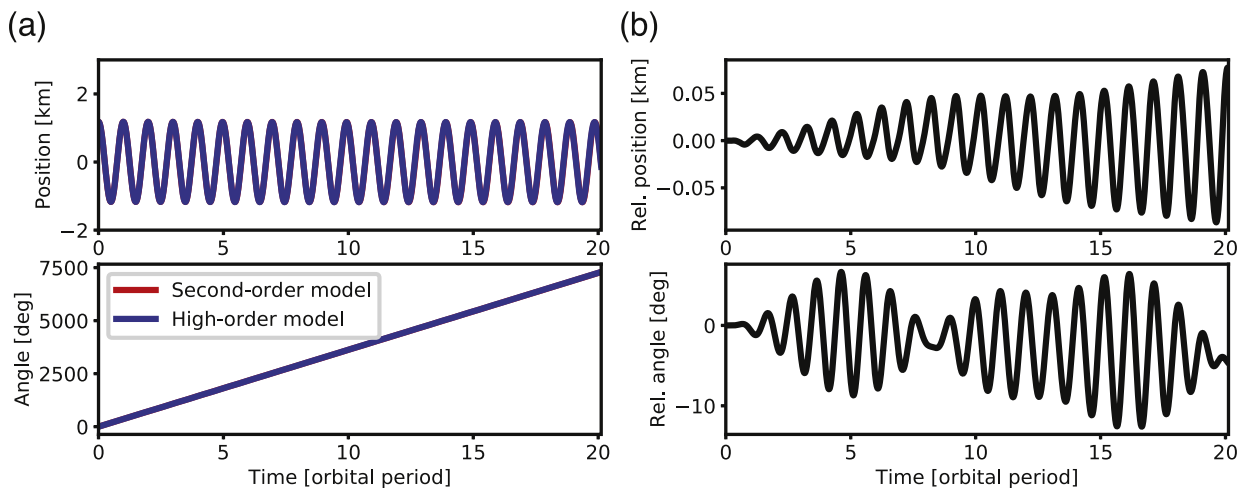


Fig. 9. Numerical simulation comparison of the second-order model and the high-order model. This figure shows the motion *after* the DART impact.  $\chi$  and  $\xi$  are defined as 0.965 and 0.65, respectively. The format is the same as Fig. 6.

driver is, again, the shapes of the modeled Didymos system. A small inconsistency in the shape models causes deviation in the rotational motion, inducing further orbital perturbation. The sensitivity of the currently used models to such complex perturbation will be explored in our future work.

#### 4.2. Analysis using the second-order model

##### 4.2.1. Effects of the primary's shape deformation and the $\beta$ parameter on the mutual orbit period change

This section explores the mutual orbit period change, taking into account shape deformation of the primary

Table 5

Simulation conditions of the second-order model for Fig. 10. The initial speed is defined using Eq. (23) to make the secondary's rotation synchronized with its orbit.

Parameters	Values	Units
$\beta$ parameter	0.5 – 2.5	[-]
Initial speed	Synchronous	m·s <sup>-1</sup>
Initial separation	1.18	km
P initial mass	$5.23 \times 10^{11}$	kg
P initial bulk density	2100	kg·m <sup>-3</sup>
P initial spin period	[-]	h
P initial oblateness	0.939	[-]
P initial shape	Spheroid	[-]
P deformation	Yes	[-]
S initial mass	$4.8 \times 10^9$	kg
S initial bulk density	2100	kg·m <sup>-3</sup>
S initial spin period	Synchronous	h
S initial elongation	1.0, 0.7	[-]
S initial shape	Ellipsoid	[-]
S deformation	No	[-]
DART mass	558	kg
DART impact speed	5.975	km·s <sup>-1</sup>
DART impact angle	15.803	deg

but fixing the elongation of the secondary. This exercise extends the work done by Hirabayashi et al. (2017). Specifically, we consider that the  $\beta$  parameter and the oblateness of the primary after the DART impact,  $\chi_a$ , are free parameters, given a constant value of the elongation of the secondary,  $\xi (= \xi_b = \xi_a)$ . The primary's oblateness before the DART impact,  $\chi_b$ , is fixed at 0.939. The conditions of the DART impact are described in Table 5. The range of the  $\beta$  parameter is between 0.5 and 2.5, covering a prediction by Walker et al. (2017), which is  $\beta = 1.0 - 1.69$ . We also investigate  $\xi = 1.0$  and 0.7 to see how the elongation of the secondary contributes to the mutual orbit period change.

Fig. 10 plots the mutual orbit period change at a given elongation of the secondary. Fig. 10(a) describes the case of  $\xi = 1.0$ . The horizontal axis is the  $\beta$  parameter, while the vertical axis is  $\chi_a$ . It is found that the magnitude of the mutual orbit period change increases when the primary's oblateness becomes small, and the  $\beta$  parameter becomes large. In the considered range ( $0.5 \leq \beta \leq 2.5$  and  $0.70 \leq \chi_a \leq 0.939$ ), the most extreme case has a mutual orbit period change of  $-45$  min; therefore, these parameters always make the mutual orbit period short.

Fig. 10(b) shows the mutual orbit period change of  $\xi = 0.7$  in comparison with that of  $\xi = 1.0$ . The general behavior is that as the elongation of the secondary increases ( $\xi$  becomes small), the mutual orbit becomes short. In the considered range of  $\xi$  and  $\beta$ , the magnitude of the relative change is up to 1.2 min. However, the largest change does not occur at the bottom-right ( $\chi_a = 0.7$  and  $\beta = 2.5$ ) but is located at  $\chi_a = 0.8$  and  $\beta = 2.5$  (Panel (b)); therefore, the difference of the mutual orbit period change does not monotonically increase when  $\chi$  decreases and  $\beta$  increases. This result indicates that the elongated sec-

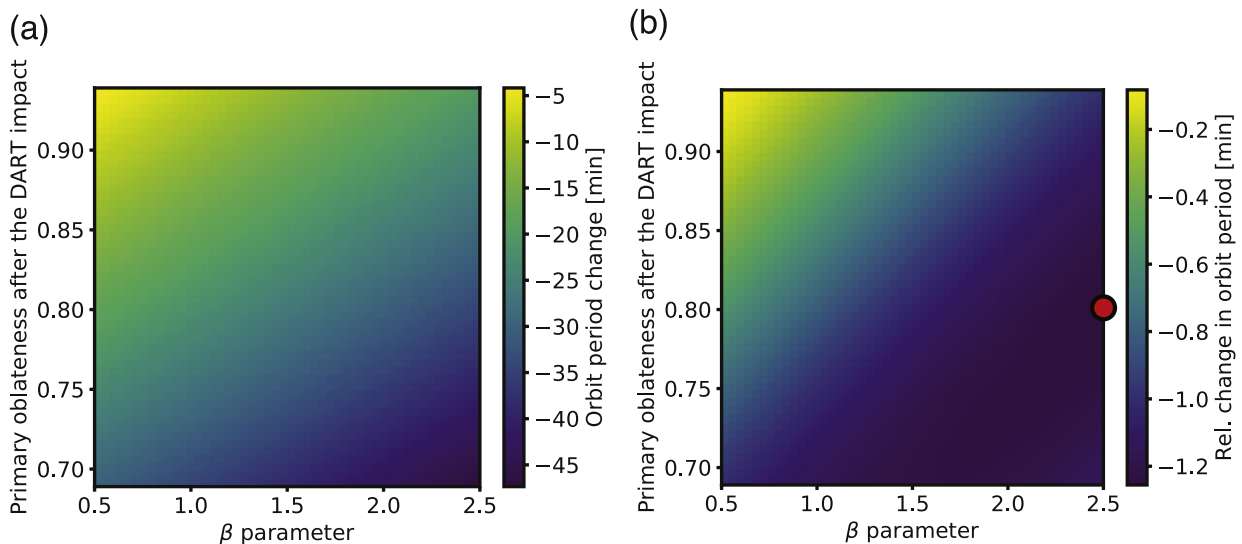


Fig. 10. Mutual orbit period change as a function of the  $\beta$  parameter and the primary's oblateness after the DART impact. Panel (a) shows the case of  $\xi = 1.0$ , while Panel (b) plots the mutual orbit period change of  $\xi = 0.7$  in comparison with that of  $\xi = 1.0$ . The red circle indicates the location of the largest change. (For interpretation of the references to colour in this figure legend, the reader is referred to the web version of this article.)

ondary’s rotation is coupled with its orbit (see Section 4.2.2).

4.2.2. Effects of the secondary’s elongation and the  $\beta$  parameter on the mutual orbit period

Here we investigate the effect of the secondary’s elongation and the  $\beta$  parameter. We do not change the oblateness of the primary,  $\chi$ , and the elongation of the secondary,  $\xi$ , before and after the DART impact.  $\chi(= \chi_b = \chi_a)$  is fixed at 0.939 through this analysis; on the other hand, we consider the range of  $\xi(= \xi_b = \xi_a)$  being between 0.5 and 1.0. Again, subscripts  $b$  and  $a$  indicate the conditions before and after the DART impact, respectively. At the initial condition, the secondary’s orbit is synchronized with its rotation. Table 6 describes the simulation settings in this exercise. Fig. 11 shows the mutual orbit period change as a function of the secondary’s elongation. We give four

Table 6  
Simulation conditions of the second-order model for Fig. 11.

Parameters	Values	Units
$\beta$ parameter	1.0, 1.5, 2.0, 2.5	[-]
Initial speed	Synchronous	m·s <sup>-1</sup>
Initial separation	1.18	km
P initial mass	$5.23 \times 10^{11}$	kg
P initial bulk density	2100	kg·m <sup>-3</sup>
P initial spin period	[-]	h
P initial oblateness	0.939	[-]
P initial shape	Spheroid	[-]
P deformation	No	[-]
S initial mass	$4.8 \times 10^9$	kg
S initial bulk density	2100	kg·m <sup>-3</sup>
S initial spin period	Synchronous	h
S initial elongation	0.5–1.0	[-]
S initial shape	Ellipsoid	[-]
S deformation	No	[-]
DART mass	558	kg
DART impact speed	5.975	km·s <sup>-1</sup>
DART impact angle	15.803	deg

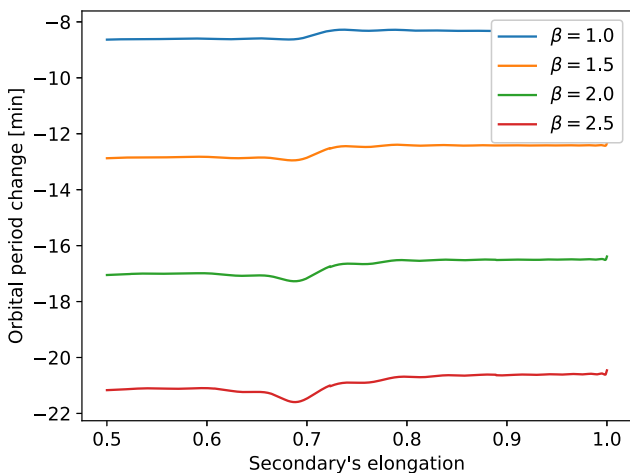


Fig. 11. Mutual orbit period change as a function of the secondary’s elongation. The lines show the results at different values of the  $\beta$  parameter.

cases of the  $\beta$  parameter: 1.0, 1.5, 2.0, and 2.5. It is found that the mutual orbit period change is almost proportional to the  $\beta$  parameter.

We see that the difference between the maximum and minimum orbit period changes at a constant value of  $\beta$  is always within 1.5 min in the range of  $\xi$  being between 0.5 and 1.0 (Fig. 11). Also, the mutual orbit period change does not proportionally evolve as a function of the secondary’s elongation. The general trend is that the mutual orbit period change is almost constant at  $\xi \gtrsim 0.72$  and  $\xi \lesssim 0.68$ . The mutual orbit period at  $\xi \lesssim 0.68$  is slightly shorter than that at  $\xi \gtrsim 0.72$ . We attribute this trend transition to the change in the orbital and rotational modes in these two regions because the secondary’s rotational oscillation (libration) correlates with its orbital motion. We also observe the peaks of the mutual orbit period change at  $\xi = 0.69$ . Fig. 12 shows the time evolution of the secondary’s orientation in three aspect ratio cases,  $\xi = 0.55, 0.69, \text{ and } 0.9$ , when  $\beta = 2.5$ . The rotation of the secondary is excited at  $\xi \approx 0.69$ . This trend changes the orbital motion, leading to different mutual orbit period changes. However, because the secondary’s mass is only 1% of the primary’s mass (the gravity from the primary is dominant), the primary’s motion is not affected by the secondary’s motion. In the considered range of  $\xi$ , therefore, although perturbation occurs in the system, its magnitude is limited. A detailed discussion of the mutual motion of a binary system was given in earlier works (e.g. Jacobson and Scheeres, 2011).

4.2.3. Effects of the secondary’s shape deformation on the mutual orbit period change

We finally discuss how the secondary’s shape deformation affects the mutual orbit period change. In this exercise, we do not consider shape deformation of the primary; its oblateness,  $\chi(= \chi_b = \chi_a)$ , is fixed at 0.939 before and after the DART impact. On the other hand, the secondary’s elongation before the DART impact,  $\xi_b$ , is not equal to

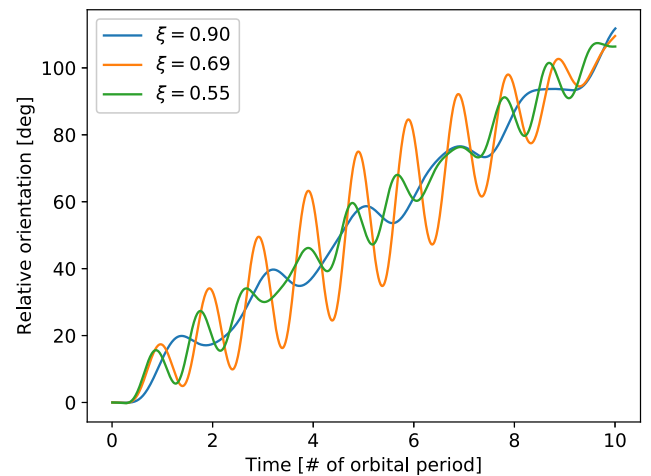


Fig. 12. Time evolution of the orientation of the secondary in 10 orbital periods. We consider three cases of  $\xi$ , 0.55, 0.69, and 0.9, under  $\beta = 2.5$ .

Table 7  
Simulation conditions of the second-order model for Fig. 13.

Parameters	Values	Units
$\beta$ parameter	1.0	[-]
Initial speed	Synchronous	$\text{m}\cdot\text{s}^{-1}$
Initial separation	1.18	km
P initial mass	$5.23 \times 10^{11}$	kg
P initial bulk density	2100	$\text{kg}\cdot\text{m}^{-3}$
P initial spin period	[-]	h
P initial oblateness	0.939	[-]
P initial shape	Spheroid	[-]
P deformation	No	[-]
S initial mass	$4.8 \times 10^9$	kg
S initial bulk density	2100	$\text{kg}\cdot\text{m}^{-3}$
S initial spin period	Synchronous	h
S initial elongation	0.85, 0.90, 0.95, 1.0	[-]
S initial shape	Ellipsoid	[-]
S deformation	Yes	[-]
DART mass	558	kg
DART impact speed	5.975	$\text{km}\cdot\text{s}^{-1}$
DART impact angle	15.803	deg

that after the DART impact,  $\xi_a$ , in this exercise. Other simulation parameters are given in Table 7. We choose four values of  $\xi_b$ : 0.85, 0.90, 0.95, and 1.0. Then, we compute the mutual orbit period change as a function of  $\xi_a$  in the range between 0.75 and 1.0 (Fig. 13). In this figure, the horizontal axis is  $\xi_a$ , while the vertical axis is the mutual orbit period change. The markers are the initial conditions of the secondary's elongation. If  $\xi_a > \xi_b$ , the secondary becomes less elongated. On the other hand, if  $\xi_a < \xi_b$ , shape deformation makes the secondary more elongated.

The results show that the variation in the secondary's aspect ratio,  $\xi$ , is a critical parameter that controls the mutual orbit period change. If the secondary becomes more elongated, i.e.,  $\xi_a$  becomes smaller than  $\xi_b$ , the mutual orbit period becomes shorter than that in the case when there is no shape deformation of the secondary. On

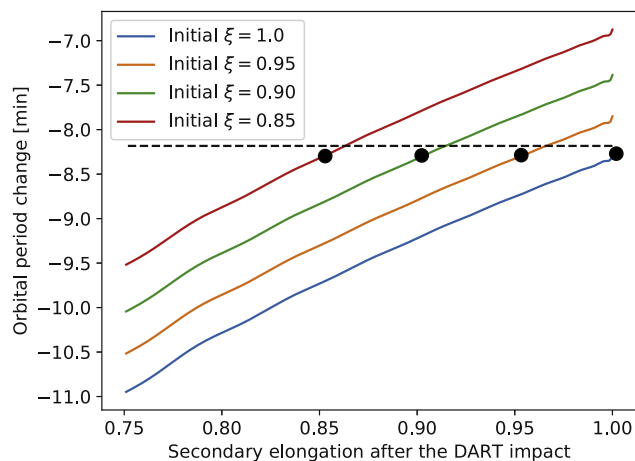


Fig. 13. Mutual orbit period change as a function of the secondary's elongation after the DART impact. Each line indicates the result for a given elongation before the DART impact. The markers give the initial elongation. The black dashed line describes the case when the primary and the secondary are spheres, which is  $-8.1832$  min from Table 2.

the other hand, if the secondary becomes less elongated, the magnitude of the mutual orbit period change becomes smaller. Because non-synchronized rotation triggered by the DART impact consumes the angular momentum of the system, this angular momentum exchange influences the relative translational motion of the secondary, causing the variations in the mutual orbit period change.

It is found that the slopes of the curves are almost similar in all the cases of  $\xi_b$ , implying that when the secondary's mass is small, the mutual orbit period change due to shape deformation is almost independent of the initial elongation of the secondary and is proportional to the magnitude of shape deformation. From the derived slopes, we compute that when the elongation changes 0.1 before and after the DART impact, the magnitude of the mutual orbit period change becomes  $\sim 1$  min. Considering the finding in Section 4.2.1, we see that while the mutual orbit period change due to the secondary's shape deformation is limited compared to that due to the primary's shape deformation, it may be critical in the DART mission, depending on the magnitude of the shape deformation process, as the mission requirement is 7.3 s for the mutual orbital period change determined by ground observations (Cheng, 2018).

## 5. Discussion

### 5.1. Consideration of high-order gravity terms

We used the shape model derived from radar observations in the high-order model, which we compared with the second-order model that only took into account the oblateness of the primary and the elongation of the secondary. The high-order model used the shapes of Didymos' primary and 1999 KW4's secondary (rescaled) and took into account their gravity terms up to fourth order. Our analysis showed that the second-order model had an error of  $\sim 10\%$  for calculation of the mutual orbit period change, compared to the high-order model (Section 4.1.3). In the present work, we made the mutual motion in the second-order model reasonably consistent with that in the high-order model by choosing proper values of the primary's oblateness,  $\chi$ , and the secondary's elongation,  $\xi$ .

However, regardless of this analysis process, the mutual orbit period change in the second-order model was not consistent with that in the high-order model. Because the difference of the mutual motion before and after the DART impact needed to be taken into account in both the second-order model and the high-order model, the mutual orbit period change could not be improved simply by choosing  $\chi$  and  $\xi$  in the second-order model. This fact implies that even though the primary is relatively spheroidal and asymmetric, the mutual motion of Didymos was complex, providing limited consistency between the second-order model and the high-order model. Thus, consideration of high-order terms of the gravity is necessary for the calculation of the mutual orbit period change.



A critical issue is that observations planned for the DART mission may be limited to determine the physical properties of Didymos such as the size, shape, and bulk density, leaving uncertainties of the  $\beta$  parameter. This fact leads to an issue that while consideration of high-order terms is critical to gravity computation, it may be difficult to determine the essential parameters for calculation of high-order gravity terms from the currently planned observations. Therefore, we emphasize that it is necessary to develop not only high-order mutual dynamics models but also simplified models and quantify how such simplified models can provide the mutual orbit period change under any circumstances with reasonable accuracy. In this sense, the second-order model may be a useful tool that achieves inexpensive computational burden and uses a limited number of free parameters. Finally, it is essential to observe this asteroid in detail to give better constraints on its physical properties. The Hera mission will provide substantial opportunities to observe Didymos and give constraints on the  $\beta$  parameter of this object.

### 5.2. Effects of the secondary's shape on the mutual orbit period change

If the secondary has an elongated shape, the orbital motion correlates with the rotational motion. Hirabayashi et al. (2017) used the shape model derived from radar observations for the primary (Naidu et al., 2016; Michel et al., 2016) but assumed the secondary to be perfectly spherical. The present work took into account the elongation of the secondary (Figs. 11 and 13). The results showed that because the elongation of the secondary would add a change in the mutual orbit period, the shape deformation process of the secondary further influences the mutual orbit period change.

Because the secondary is no longer spherical in the present work, the rotational condition is a crucial parameter to investigate the mutual dynamics of Didymos. In the simulations performed in this study, the secondary's rotation is assumed to be initially synchronized with its orbital state. Pravec et al. (2016) argued that for binary asteroids with orbital periods shorter than 20 h, many of them have secondaries in 1:1 synchronous spin states. Also, most of the synchronous secondaries showed librations with a small amplitude ( $\leq 20$  deg). Therefore, this assumption may be reasonable for the mutual dynamics of Didymos.

The DART spacecraft is planned to impact the center of figure of the secondary and provide minimized torque acting on the secondary. Thus, while its orbit period becomes shorter after the DART impact, the secondary's rotational period is not expected to change. Thus, the rotational motion may be delayed from the orbital motion. This process transfers angular momentum from the rotational motion to the orbital motion, which provides further acceleration of the orbital motion. We demonstrated that the mutual orbit period change would depend on the elongation of the secondary; however, the magnitude of the elon-

gation is less understood because of limited observational constraints (Pravec et al., 2006).

The shape deformation process of the secondary controls the mutual orbit period change. When the secondary deforms, the inertia integrals change. Due to the mutual interaction between orbit and rotation, the shape deformation process causes stronger libration than the case when the secondary has no deformation. When the secondary becomes less elongated than the original case, the mutual orbit period becomes longer. On the other hand, when the secondary becomes more elongated, the mutual orbit period becomes shorter. These conditions result from a transfer of the angular momentum between the secondary's rotation and its orbit. Unlike the shape deformation process of the primary, which is mainly controlled by the centrifugal force, the deformation process of the secondary may be controlled by the DART impact process under the assumption that the secondary is tidally locked.

### 5.3. Necessity of identifying the shape-deformation scenario's probability

We address that the present study and the previous work done by Hirabayashi et al. (2017) do not provide a probability of whether the DART impact triggers the proposed scenarios. The probability of this process highly depends on the deformation process of Didymos. For the primary, although Zhang et al. (2017) and Hirabayashi et al. (2017) argued the primary's sensitivity to structural or surface failure, these works agreed that this sensitivity would be dependent on the internal structure. If the structure has high mechanical strength, it is likely that the primary holds its original shape (e.g. Rozitis et al., 2014; Hirabayashi and Scheeres, 2014; Hirabayashi, 2015; Sánchez and Scheeres, 2016; Zhang et al., 2018). However, if the structure is weak, the internal structure controls the magnitude and mode of shape deformation.

Investigations require sophisticated skills and knowledge for the impact process to give constraints on the magnitude of the secondary's shape deformation. Once a projectile hits a terrestrial surface, the shock wave propagates through the surface and crushes material (Melosh, 1989). A critical issue is that impact conditions highly depend on the surface topography of a target asteroid (Bruck Syal et al., 2016; Stickle et al., 2017; Tatsumi and Sugita, 2018). The Deep Impact mission that demonstrated an impactor colliding with comet Tempel 1 showed that impact-generated ejecta on a small body might be dependent on the subsurface porosity and obliquity (A'Hearn et al., 2005). An experimental study showed that an oblique impact generated a transient crater normal to the surface topography, and the surface orientation controls the direction of its ejecta curtain (Aschauer and Kenkmann, 2017). Thus, if the DART impactor hits a slope, asymmetric ejecta may contribute to a change in the angular momentum of the secondary, possibly causing the spin state evolution. When an impact crater forms on a porous surface,

strong compaction may occur beneath its transient crater (Wünnemann et al., 2006; Collins, 2014). Recent work also considered tensile failure during the impact formation, proposing that the porosity variation would occur even in regions far from the impact site (Wiggins et al., 2018).

In addition to proposing the effect of the primary's shape deformation on the mutual orbit period change, our work addresses an issue of possible shape deformation of the secondary. The DART impact process is a main driver that causes the secondary to have landslides or shape deformation. Taking into account the 7.3-s DART requirement for ground observations of the mutual orbit period change (Cheng, 2018), we obtain the minimum thickness of a surface movement that causes a mutual orbit period change higher than the 7.3-s requirement as 70 cm. Consideration of shape deformation of the Didymos system requires a detailed understanding of topographic deformation processes, as well as information on the physical properties of Didymos. Sophisticated impact analyses are necessary to identify the probability of whether Didymos experiences shape deformation induced by the DART impact. Such investigations provide constraints on the mutual dynamics of Didymos, allowing for better estimation of the  $\beta$  parameter.

## 6. Conclusion

We investigated how the mutual orbit period change of binary near-Earth asteroid (65803) Didymos would be affected by the original shape and the shape deformation process due to the DART impact. In this work, we mainly used the second-order inertia-integral mutual dynamics model that assumed the primary and the secondary to be an oblate spheroid and a prolate ellipsoid, respectively. This second-order model was compared with a two-body-problem-based model, a polyhedron-shape-based mutual dynamics model that took into account the shape of Didymos' primary and a spherical secondary, and a high-order inertia-integral mutual dynamics model that adopted Didymos' primary and 1999 KW4's secondary. The second-order model produced results consistent with the sphere-sphere model and the polyhedron-shape mutual dynamics model when the primary's deformation is small. On the other hand, this model had an error of  $\sim 10\%$  for the computation of the mutual orbit period change, compared to the high-order inertia-integral mutual dynamics model that considered the gravity terms up to fourth order. We then analyzed the effects of the shapes on the mutual period change. The results showed that the mutual orbit period change was dependent on the shape condition. This study suggests that the original shapes and shape deformation due to the DART impact may play significant roles in changing the mutual orbit period of Didymos, which may affect the detailed assessment of the  $\beta$  parameter in the AIDA mission. Further investigation shed light on the detailed mechanism of the DART impact, providing a better estimate of the  $\beta$  parameter.

## Acknowledgements

This work is conducted under Phase C/D of the NASA DART mission. M.H. acknowledges support from the Department of Aerospace Engineering at Auburn University. A.B.D. thanks support from the National Science Foundation Graduate Research Fellowship Program under Grant No. DGE 1650115. P.P. was supported by the Grant Agency of the Czech Republic, Grant 17-00774S. This work is supported by the NASA DART mission.

## References

- A'Hearn, M.F., Belton, M.J.S., Delamere, W.A., Kissel, J., Klaasen, K.P., McFadden, L.A., Meech, K.J., Melosh, H.J., Schultz, P.H., Sunshine, J.M., Thomas, P.C., Veverka, J., Yeomans, D.K., Baca, M.W., Busko, I., Crockett, C.J., Collins, S.M., Desnoyer, M., Eberhardy, C.A., Ernst, C.M., Farnham, T.L., Feaga, L., Groussin, O., Hampton, D., Ipatov, S.I., Li, J., Lindler, D., Lisse, C.M., Mastrodemos, N., Owen Jr., W.M., Richardson, J.E., Wellnitz, D.D., White, R.L., 2005. Deep impact: excavating comet Tempel 1. *Science* 310, 258–264. <https://doi.org/10.1126/science.1118923>.
- Aschauer, J., Kenkmann, T., 2017. Impact cratering on slopes. *Icarus* 290, 89–95. <https://doi.org/10.1016/j.icarus.2017.09.021>.
- Bruck Syal, M., Owen, J.M., Miller, P.L., 2016. Deflection by kinetic impact: sensitivity to asteroid properties. *Icarus* 269, 50–61. <https://doi.org/10.1016/j.icarus.2016.01.010>.
- Cheng, A., 2018. AIDA DART mission: double asteroid redirection test. In: *The 9th Catastrophic Disruption Workshop*.
- Cheng, A., Michel, P., Jutzi, M., Rivkin, A., Stickle, A., Barnouin, O., Ernst, C., Atchison, J., Pravec, P., Richardson, D., et al., 2016. Asteroid impact & deflection assessment mission: kinetic impactor. *Planet. Space Sci.* 121, 27–35. <https://doi.org/10.1016/j.pss.2015.12.004>.
- Cheng, A.F., Rivkin, A.S., Michel, P., Atchison, J., Barnouin, O., Benner, L., Chabot, N.L., Ernst, C., Fahnestock, E.G., Kueppers, M., Pravec, P., Rainey, E., Richardson, D.C., Stickle, A.M., Thomas, C., 2018. AIDA DART asteroid deflection test: planetary defense and science objectives. *Planet. Space Sci.* 157, 104–115. <https://doi.org/10.1016/j.pss.2018.02.015>.
- Collins, G.S., 2014. Numerical simulations of impact crater formation with dilatancy. *J. Geophys. Res.: Planets* 119, 2600–2619. <https://doi.org/10.1002/2014JE004708>.
- Davis, A.B., Scheeres, D.J., 2017. Binary asteroid orbit sensitivity to gravity field coefficients: applications to the AIDA mission target 65803 Didymos. In: *Lunar and Planetary Science Conference*, p. 1299.
- Fahnestock, E.G., Scheeres, D.J., 2006. Simulation of the full two rigid body problem using polyhedral mutual potential and potential derivatives approach. *Celestial Mech. Dyn. Astron.* 96, 317–339. <https://doi.org/10.1007/s10569-006-9045-5>.
- Feldhacker, J.D., Syal, M.B., Jones, B.A., Doostan, A., McMahon, J.W., Scheeres, D.J., 2017. Shape dependence of the kinetic deflection of asteroids. *J. Guid. Control Dyn.* 40, 2417–2431. <https://doi.org/10.2514/1.G002270>.
- Goldreich, P., Sari, R., 2009. Tidal evolution of rubble piles. *Astrophys. J.* 691, 54–60. <https://doi.org/10.1088/0004-637X/691/1/54>.
- Hirabayashi, M., 2015. Failure modes and conditions of a cohesive, spherical body due to YORP spin-up. *Monthly Not. Roy. Astronom. Soc.* 454, 2249–2257. <https://doi.org/10.1093/mnras/stv2017>.
- Hirabayashi, M., Scheeres, D.J., 2013. Recursive computation of mutual potential between two polyhedra. *Celestial Mech. Dyn. Astron.* 117, 245–262. <https://doi.org/10.1007/s10569-013-9511-x>.
- Hirabayashi, M., Scheeres, D.J., 2014. Stress and failure analysis of rapidly rotating asteroid (29075) 1950 DA. *Astrophys. J. Lett.* 798, L8. <https://doi.org/10.1088/2041-8205/798/1/L8>.

- Hirabayashi, M., Schwartz, S.R., Yu, Y., Davis, A.B., Chesley, S.R., Fahnestock, E.G., Michel, P., Richardson, D.C., Naidu, S.P., Scheeres, D.J., Cheng, A.F., Rivkin, A.S., Benner, L.A.M., 2017. Constraints on the perturbed mutual motion in Didymos due to impact-induced deformation of its primary after the DART impact. *Monthly Not. Roy. Astron. Soc.* 472, 1641–1648. <https://doi.org/10.1093/mnras/stx1992>.
- Holsapple, K.A., Housen, K.R., 2012. Momentum transfer in asteroid impacts. I. Theory and scaling. *Icarus* 221, 875–887. <https://doi.org/10.1016/j.icarus.2012.09.022>.
- Hou, X., Scheeres, D.J., Xin, X., 2017. Mutual potential between two rigid bodies with arbitrary shapes and mass distributions. *Celest. Mech. Dyn. Astron.* 127, 369–395. <https://doi.org/10.1007/s10569-016-9731-y>.
- Jacobson, S.A., Scheeres, D.J., 2011. Dynamics of rotationally fissioned asteroids: Source of observed small asteroid systems. *Icarus* 214, 161–178. <https://doi.org/10.1016/j.icarus.2011.04.009>.
- Maciejewski, A.J., 1995. Reduction, relative equilibria and potential in the two rigid bodies problem. *Celest. Mech. Dyn. Astron.* 63, 1–28. <https://doi.org/10.1007/BF00691912>.
- McMahon, J.W., Scheeres, D.J., 2013. Dynamic limits on planar libration-orbit coupling around an oblate primary. *Celest. Mech. Dyn. Astron.* 115, 365–396. <https://doi.org/10.1007/s10569-012-9469>.
- Melosh, H.J., 1989. *Impact Cratering: A Geologic Process*. Research Supported by NASA. Oxford University Press, New York (Oxford Monographs on Geology and Geophysics, No. 11), 253 p. 11.
- Michel, P., Cheng, A., Küppers, M., Pravec, P., Blum, J., Delbo, M., Green, S.F., Rosenblatt, P., Tsiganis, K., Vincent, J.B., Biele, J., Ciarletti, V., Hérique, A., Ulamec, S., Carnelli, I., Galvez, A., Benner, L., Naidu, S.P., Barnouin, O.S., Richardson, D.C., Rivkin, A., Scheirich, P., Moskovitz, N., Thirouin, A., Schwartz, S.R., Campo Bagatin, A., Yu, Y., 2016. Science case for the Asteroid Impact Mission (AIM): a component of the Asteroid Impact & Deflection Assessment (AIDA) mission. *Adv. Space Res.* 57, 2529–2547. <https://doi.org/10.1016/j.asr.2016.03.031>.
- Michel, P., Kueppers, M., Sierks, H., Carnelli, I., Cheng, A.F., Mellab, K., Granvik, M., Kestilä, A., Kohout, T., Muinonen, K., Näsilä, A., Penttilä, A., Tikka, T., Tortora, P., Ciarletti, V., Hérique, A., Murdoch, N., Asphaug, E., Rivkin, A., Barnouin, O., Bagatin, A.C., Pravec, P., Richardson, D.C., Schwartz, S.R., Tsiganis, K., Ulamec, S., Karatekin, O., 2018. European component of the AIDA mission to a binary asteroid: characterization and interpretation of the impact of the DART mission. *Adv. Space Res.* 62 (8), 2261–2272. <https://doi.org/10.1016/j.asr.2017.12.020>.
- Naidu, S.P., Benner, L., Brozovic, M., Ostro, S.J., Nolan, M.C., Margot, J.L., Giorgini, J.D., Magri, C., Pravec, P., Scheirich, P., Scheeres, D.J., Hirabayashi, M., 2016. Observations and characterization of binary near-earth asteroid 65803 Didymos, the Target of the AIDA Mission. In: *Fall Meeting of American Geophysical Union*, pp. P52B-02.
- Ostro, S.J., Margot, J.L., Benner, L.A.M., Giorgini, J.D., Scheeres, D.J., Bellerose, J., Nolan, M.C., Magri, C., Pravec, P., Scheirich, P., Rose, R., Jurgens, R.F., De Jong, E.M., Suzuki, S., 2006. Radar imaging of binary near-earth asteroid (66391) 1999 KW4. *Science* 314, 1276–1280. <https://doi.org/10.1126/science.1133622>.
- Pravec, P., Scheirich, P., Kušnirák, P., Šarounová, L., Mottola, S., Hahn, G., Brown, P., Esquerdo, G., Kaiser, N., Krzeminski, Z., Pray, D.P., Warner, B.D., Harris, A.W., Nolan, M.N., Howell, E.S., Benner, L.A.M., Margot, J.L., Galád, A., Holliday, W., Hicks, M.D., Krugly, Y.N., Tholen, D., Whiteley, R., Marchis, F., DeGraff, D.R., Grauer, A., Larson, S., Velichko, F.P., W.R.C. Jr., Stephens, R., Zhu, J., Kirsch, K., Dyvig, R., Snyder, L., Reddy, V., Moore, S., Gajdos, S., Világi, J., Masi, G., Higgins, D., Funkhouser, G., Knight, B., Slivan, S., Behrend, R., Grenon, M., Burki, G., Roy, R., Demeautis, C., Matter, D., Waelchli, N., Revas, Y., Klotz, A., Rieugné, M., Thierry, P., Cotrez, V., Brunetto, L., Kober, G., 2006. Photometric survey of binary near-Earth asteroids. *Icarus* 181, 63–93. <https://doi.org/10.1016/j.icarus.2005.10.014>.
- Pravec, P., Scheirich, P., Kušnirák, P., Hornoch, K., Galád, A., Naidu, S. P., Pray, D.P., Világi, J., Gajdos, Š., Krugly, Y.N., Cooney, W.R., Gross, J., Terrell, D., Gaftonyuk, N., Pollock, J., Husárik, M., Chiorny, V., Stephens, R.D., Durkee, R., Reddy, V., Dyvig, R., Vrástíl, J., Žizka, J., Mottola, S., Hellmich, S., Oey, J., Benishek, V., Kryszyńska, A., Higgins, D., Ries, J., Marchis, F., Baek, M., Macomber, B., Inasaridze, R., Kvaratskhelia, O., Ayvazian, V., Rumyanstev, V., Masi, G., Colas, F., Lecacheux, J., Montaigut, R., Leory, A., Brown, P., Krzeminski, Z., Molotov, I., Reichart, D., Haislip, J., LaCluyze, A., 2016. Binary asteroid population. 3. Secondary rotations and elongations. *Icarus* 267, 267–295. <https://doi.org/10.1016/j.icarus.2015.12.019>.
- Richardson, D.C., Michel, P., Walsh, K.J., Flynn, K.W., 2009. Numerical simulations of asteroids modelled as gravitational aggregates with cohesion. *Planet. Space Sci.* 57, 183–192. <https://doi.org/10.1016/j.pss.2008.04.015>.
- Rozitis, B., MacLennan, E., Emery, J.P., 2014. Cohesive forces prevent the rotational breakup of rubble-pile asteroid (29075) 1950 DA. *Nature* 512, 174–176. <https://doi.org/10.1038/nature13632>.
- Sánchez, D.P., Scheeres, D.J., 2012. DEM simulation of rotation-induced reshaping and disruption of rubble-pile asteroids. *Icarus* 218, 876–894. <https://doi.org/10.1016/j.icarus.2012.01.014>.
- Sánchez, P., Scheeres, D.J., 2016. Disruption patterns of rotating self-gravitating aggregates: a survey on angle of friction and tensile strength. *Icarus* 271, 453–471. <https://doi.org/10.1016/j.icarus.2016.01.016>.
- Scheeres, D.J., 2002. Stability in the full two-body problem. *Celest. Mech. Dyn. Astron.* 83, 155–169. [https://doi.org/10.1007/978-94-017-2304-6\\_10](https://doi.org/10.1007/978-94-017-2304-6_10).
- Scheeres, D.J., 2009. Stability of the planar full 2-body problem. *Celest. Mech. Dyn. Astron.* 104, 103–128. <https://doi.org/10.1007/s10569-009-9184-7>.
- Scheeres, D.J., Fahnestock, E.G., Ostro, S.J., Margot, J.L., Benner, L.A. M., Broschart, S.B., Bellerose, J., Giorgini, J.D., Nolan, M.C., Magri, C., Pravec, P., Scheirich, P., Rose, R., Jurgens, R.F., De Jong, E.M., Suzuki, S., 2006. Dynamical configuration of binary near-earth asteroid (66391) 1999 KW4. *Science* 314, 1280–1283. <https://doi.org/10.1126/science.1133599>.
- Stickley, A.M., Rainey, E.S.G., Bruck Syal, M., Owean, J.M., Miller, P., Barnouin, O.S., Ernst, C.M. the AIDA Impact Simulation Working Group, 2017. Modeling impact outcomes for the double asteroid redirection test (dart) mission. *Proc. Eng.* 204, 116–123. <https://doi.org/10.1016/j.proeng.2017.09.763>, 14th Hypervelocity Impact Symposium 2017, HVIS2017, 24–28 April 2017, Canterbury, Kent, UK.
- Stickley, A.M., Rainey, E.S.G., Owen, J.M., Raducan, S.D., Bruck Syal, M., Collins, G.S., Davison, T.M., Miller, P.L. the DART Impact Modeling and Simulation Working Group, 2018. Modeling momentum enhancement from impact into rubble pile asteroids. In: *Lunar and Planetary Science Conference*, p. 1576.
- Tatsumi, E., Sugita, S., 2018. Cratering efficiency on coarse-grain targets: implications for the dynamical evolution of asteroid 25143 Itokawa. *Icarus* 300, 227–248. <https://doi.org/10.1016/j.icarus.2017.09.004>.
- von Braun, C., 1991. *On the gravitational potential of two arbitrary rotating bodies with applications to the Earth-Moon system* Ph.D. thesis. University of Texas at Austin.
- Walker, J.D., Chocron, S., Grosch, D.J., Durda, D.D., Housen, K.R., 2017. Momentum enhancement due to hypervelocity impacts into pumice. *Proc. Eng.* 204, 130–137. <https://doi.org/10.1016/j.proeng.2017.09.765>, 14th Hypervelocity Impact Symposium 2017, HVIS2017, 24–28 April 2017, Canterbury, Kent, UK.
- Walsh, K.J., Richardson, D.C., Michel, P., 2008. Rotational breakup as the origin of small binary asteroids. *Nature* 454, 188–191. <https://doi.org/10.1038/nature07078>.
- Werner, R.A., Scheeres, D.J., 1997. Exterior gravitation of a polyhedron derived and compared with harmonic and mascon gravitation representation of asteroid 4769 Castalia. *Celest. Mech. Dyn. Astron.* 65, 313–344. <https://doi.org/10.1007/BF00053511>.

- Werner, R.A., Scheeres, D.J., 2005. Mutual potential of homogeneous polyhedra. *Celest. Mech. Dyn. Astron.* 91, 337–349. <https://doi.org/10.1007/s10569-004-4621-0>.
- Wiggins, S.E., Johnson, B.C., Collins, G.S., Bowling, T.J., Melosh, H.J., 2018. Impact-generated porosity at depth within the lunar crust. In: *Lunar and Planetary Science Conference*, p. 2157.
- Wünnemann, K., Collins, G.S., Melosh, H.J., 2006. A strain-based porosity model of ruse in hydrocode simulations of impacts and implications for transient crater growth in porous targets. *Icarus* 180, 514–527. <https://doi.org/10.1016/j.icarus.2005.10.013>.
- Yu, Y., Michel, P., 2018. Ejecta cloud from the AIDA space project kinetic impact on the secondary of a binary asteroid: II. Fates and evolutionary dependencies. *Icarus* 312, 128–144. <https://doi.org/10.1016/j.icarus.2018.04.017>.
- Yu, Y., Michel, P., Schwartz, S.R., Naidu, S.P., Benner, L.A., 2017. Ejecta cloud from the AIDA space project kinetic impact on the secondary of a binary asteroid: I. mechanical environment and dynamical model. *Icarus* 282, 313–325. <https://doi.org/10.1016/j.icarus.2016.09.008>.
- Zhang, Y., Richardson, D.C., Barnouin, O.S., Maurel, C., Michel, P., Schwartz, S.R., Ballouz, R.L., Benner, L.A., Naidu, S.P., Li, J., 2017. Creep stability of the proposed AIDA mission target 65803 Didymos: I. Discrete cohesionless granular physics model. *Icarus* 294, 98–123. <https://doi.org/10.1016/j.icarus.2017.04.027>.
- Zhang, Y., Richardson, D.C., Barnouin, O.S., Michel, P., Schwartz, S.R., Ballouz, R.L., 2018. Rotational failure of rubble-pile bodies: influences of shear and cohesive strengths. *Astrophys. J.* 857, 15–20. <https://doi.org/10.3847/1538-4357/aab5b2>.